Batteries & Supercaps

Review
doi.org/10.1002/batt.202400823

Chemistry Europe
European Chemical
Societies Publishing

www.batteries-supercaps.org

Group IVA Alloy Anodes for Sodium-Ion Rechargeable Batteries: Electrochemistry, Mechanics, and Kinetics

Jia Zhang[a] and Tianye Zheng*[a, b]

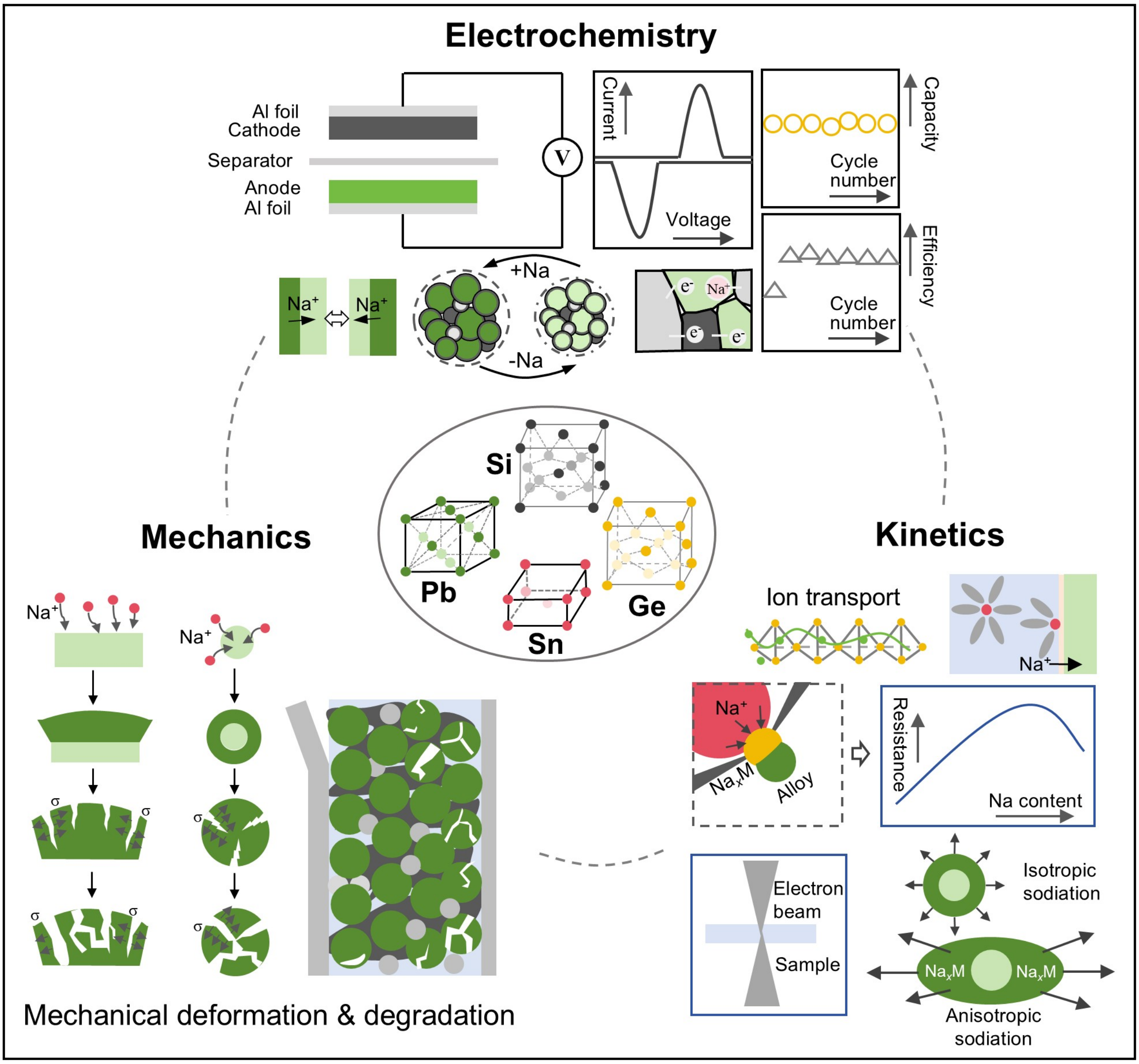

Sodium-ion batteries (SIBs) are perhaps the most promising technology currently to fulfill the requirements of large-scale energy storage. Unlike lithium, sodium (Na) source is cost-effective, abundant, and geographically evenly distributed. While hard carbon remains the benchmark anode material in SIBs, its specific capacity is limited by adsorption-intercalation chemistry, necessitating the exploration of new alternatives to meet the increasing energy demands. Group IVA alloy elements exhibit interesting sodium storage capabilities with significantly higher specific capacities. This work systematically reviews the electrochemistry, mechanics, and kinetics of silicon (Si), germanium (Ge), tin (Sn), and lead (Pb) in various SIB systems, highlighting the key points of each element: (1) Si is electrochemically inactive to Na though theoretical calculations suggest the existence of Na–Si intermetallic compounds; (2) the formation of Na–Ge phases beyond 1 : 1 atomic stoichiometry is kinetically limited; (3) the high impedance of Na–Sn phases lead to a series of charge transfer issues; (4) Pb-based anodes should not be fully eliminated from the future roadmap due to the promising cycling performances and mature recycling efforts. Collectively, this review sets a comprehensive foundation for researchers investigating alloy-type anodes for SIBs.

1. Introduction

The successful commercialization of lithium-ion batteries (LIBs) in the early 1990s facilitated a societal transformation by enabling the revolution of smartphones and consumer electronics. Thanks to LIBs, electric vehicles (EVs) have been undergoing an extraordinarily fast development in the past decade. LIB technology is also transforming towards an even larger scale, providing electric energy storage solutions for power grids in populated municipalities with off-peak electricity and/or in decentralized areas with intermittent renewable power sources. At the moment, there is almost no question that the deployment of LIBs is the best option for these energy storage practices. The increasing demand for LIBs, however, remains controversial as it may introduce social, political, and environmental risks, e.g., during lithium extraction and cobalt mining.[1] Some governments and enterprises have been worrying about the supply bottleneck of the key materials involved in LIB manufacturing, which may be caused by geographically uneven distributions and uncertain political situations. Therefore, people are identifying possible alternatives to LIBs, where lithium (Li) is not an essential element, referring to post-Li batteries based on sodium (Na), potassium (K), magnesium (Mg), aluminum (Al), and so forth.[2] Generally, these post-lithium technologies could potentially deliver higher energy densities, and be more cost-effective, environmentally friendly, and sustainable. Among them, sodium-ion batteries (SIBs) are perhaps the most promising candidate, especially since SIBs have already been introduced into the markets, albeit with limited applications primarily focused on large-scale energy storage instead of directly competing with LIBs. SIB chemistry also enables the use of oxides or polyanionic compounds that are free of cobalt and even nickel, suggesting a fundamentally different economic landscape compared to LIBs.

SIBs started drawing researchers' attention almost the same time as LIBs since the discovery of sodium beta alumina which laid the foundation of solid-state chemistry and the invention of modern LIBs.[3] A historical diagram is given in Figure 1, highlighting the key milestones in the development of SIBs. The effort to develop SIBs was largely discontinued in the early 1990s when Sony introduced the very first generation of commercial LIB products.[4] After a series of revisits in recent years, SIBs are well-recognized by both academia and industry as a promising solution for (large-scale) electric energy storage, owing to the advantages of abundant sodium source,[5] reduced material cost,[6] and zero-volt stability.[7] The current situation of SIBs is evidenced by the increasing number of scientific publications and the popularity of commercial products. Layered oxides, polyanionic phosphates, and Prussian blue analogs (PBAs) have been showing promises in functioning as the positive electrodes in SIBs,[5] and can be seen in commercial products from Faradion Ltd., the UK, HiNa Battery Technology Co., Ltd., China, and CATL, China. Nevertheless, candidates for negative electrodes seem more restricted, leaving carbonaceous materials (i.e., hard carbon; HC) the most promising ones, especially when their precursors are derived from low-cost biowaste.[8] While HC exhibits acceptable sodium storage capability, its adsorption-intercalation chemistry limits the capacity, giving a theoretical value of ca. 350 $\mathrm{mAh\,g^{-1}}$.[9] Theoretically, larger Na (than Li) ions necessitate the numerous defect sites in HC (a lower degree of graphitization) to facilitate easier Na migration. However, these defects can trap quite a few Na atoms upon the initial sodiation, resulting in poor initial coulombic efficiency (ICE). Zhang et al. reviewed 22 studies of HC anodes in SIBs, where a wide range of ICEs are reported. The ICE values can be as high as 92% or as low as 27% depending on the precursors and synthesis methods of HC.[10] Ultimately, commercially available HC anodes prepared for SIBs often deliver specific capacities of 240–250 $\mathrm{mAh\,g^{-1}}$ (e.g., NEI Corporation, MSE Supplies LLC, and Xiamen TOB New Energy Technology Co., Ltd.). As a result, seeking better anodes with higher ICEs for SIBs is necessary.

Aside from HC, several other anode candidates for SIBs exist, each characterized by distinct sodium storage mechanisms, including alloying, conversion, and alloying-conversion types.[2]

---

[a] *J. Zhang, T. Zheng*
Department of Electrical and Electronic Engineering, The Hong Kong Polytechnic University, Hung Hom, Kowloon, Hong Kong

[b] *T. Zheng*
Photonics Research Institute, The Hong Kong Polytechnic University, Hung Hom, Kowloon, Hong Kong
E-mail: darren.ty.zheng@connect.polyu.hk
t1zheng@polyu.edu.hk

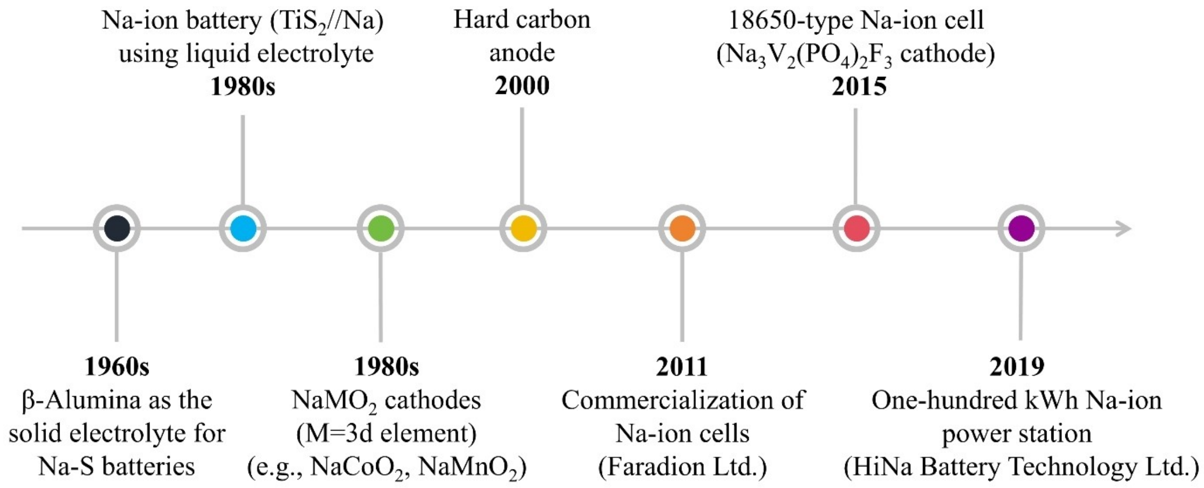

Figure 1. The historical diagram of electrode materials and cell designs for SIBs.[11]

Among them, alloy anode candidates can offer attractive theoretical capacities, which originate from the formation of various Na-containing intermetallic compounds, but with more pronounced volume expansions. Furthermore, the energy required for bond-breaking in old phases and for the nucleation/growth of new phases varies, leading to shifts in chemical potentials,[12] subsequently affecting the ionic/electric conductivities of these sodiated phases. These phase transformations may also impact electrode integrity since the electrochemical and mechanical properties of each intermetallic phase can be different.[13] Together, these (de−)alloying processes can lead to a series of problems, such as structural change, physical damage, and mechanical stress, all of which are well-documented in alloy anodes for LIBs,[14] but seem to remain elusive in that for SIBs. Additionally, the solid-electrolyte interphase (SEI) in SIBs is often less stable than that in LIBs and may redissolve in liquid electrolytes due to its higher solubility in organic carbonate solvents, leading to more susceptible SEI destruction.[15]

This paper therefore focuses on reviewing the research progress of alloy anodes in SIBs, aiming to provide relevant information for seeking anode alternatives to the current state-of-the-art HC. A special emphasis is given to the Group IVA elements, all of which can (potentially) be sodiated, but Sn seems the only alloy anode candidate that draws people's attention in the SIB field.[16] Owing to the chemical similarities, the fundamentals of each element during (de-)sodiation are carefully compared, to better shed light on their behaviors as anode materials in SIBs. We write this article following a step-by-step approach, starting with the elements from top to bottom in the periodic table, and trying to discuss their analogies and contrasts in Na storage behavior. Although this report covers most studies of the pure elemental anodes, including both theoretical and experimental efforts, we apologize in advance for any references overlooked or omitted like multi-element alloy or metal-carbon blends.

2. Anode Materials for Sodium-Ion Batteries

Like the LIB system, many chemical elements can alloy with Na at low electric potentials vs. Na/Na^+ to form intermetallic compounds. Most of these elements belong to Group IIIA, IVA, VA, and VIA of the periodic table (Figure 2). We have selected several typical alloy anodes in SIBs from the existing literature and summarized their characteristics, challenges, and strategies for improvements. These anode candidates generally exhibit higher specific capacities, such as 600–1814 $mAh\,g^{-1}$ for phosphorus,[17] ~540-600 $mAh\,g^{-1}$ for antimony,[18] and ~392-452 $mAh\,g^{-1}$ for bismuth.[19] However, the incorporation of larger Na^+ (than Li^+) often induces larger volume changes and poorer reaction kinetics, leading to unstable electrochemical

Jia Zhang just received her doctorate from The Hong Kong Polytechnic University (PolyU) in 2025. She obtained her bachelor's degree from Hunan University of Science and Technology and her master's degree from Central South University. She has also worked as a lecturer for years in Pingxiang University, China. Her ongoing research focuses on the mechanism and kinetics of phase transformations in battery materials, and the electrode/electrolyte interfaces in Li-/Na-ion batteries.

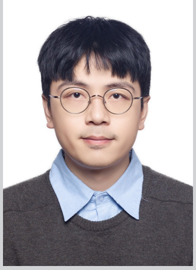

Tianye (Darren) Zheng is currently a Postdoctoral Fellow at the Hong Kong Polytechnic University (PolyU), where he received his doctorate in 2021. His early degrees were obtained from Avans University of Applied Sciences and Wageningen University in the Netherlands. He has conducted research in countries like Canada, Finland, and Germany. His research interests cover Li-/Na-ion battery chemistries, capacitive devices, and operando sensing techniques for electrochemical cells.

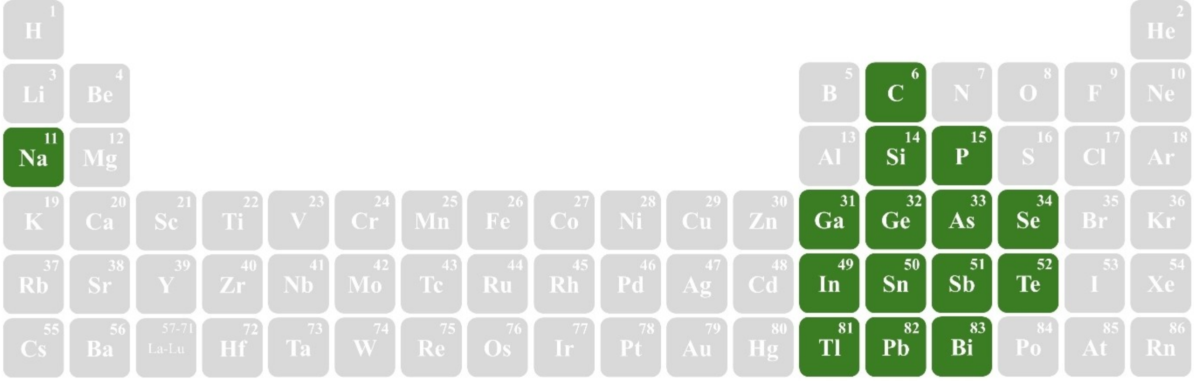

Figure 2. The periodic table highlighting the elements that can form alloys (deposition for Na; adsorption/intercalation for C) with Na from different chemical groups. Transition metal elements are excluded.

performances. Consequently, researchers have been trying to mitigate these issues via engineering efforts (Figure 3). In addition to the elements highlighted in Figure 2, it should be noted that sulfur stores Na at a relatively high potential versus Na/Na$^+$, thus functioning as the cathode in SIBs. Aluminum exhibits promising features in LIB systems,[20] but seems inactive to Na, explaining why aluminum foil is used in SIBs as the current collectors for both electrodes. At the end of the day, Group IVA is perhaps the only chemical group, in which all elements can (potentially) be both lithiated and sodiated.

Since the experimental results do not always report the same capacities, we have calculated the theoretical capacities

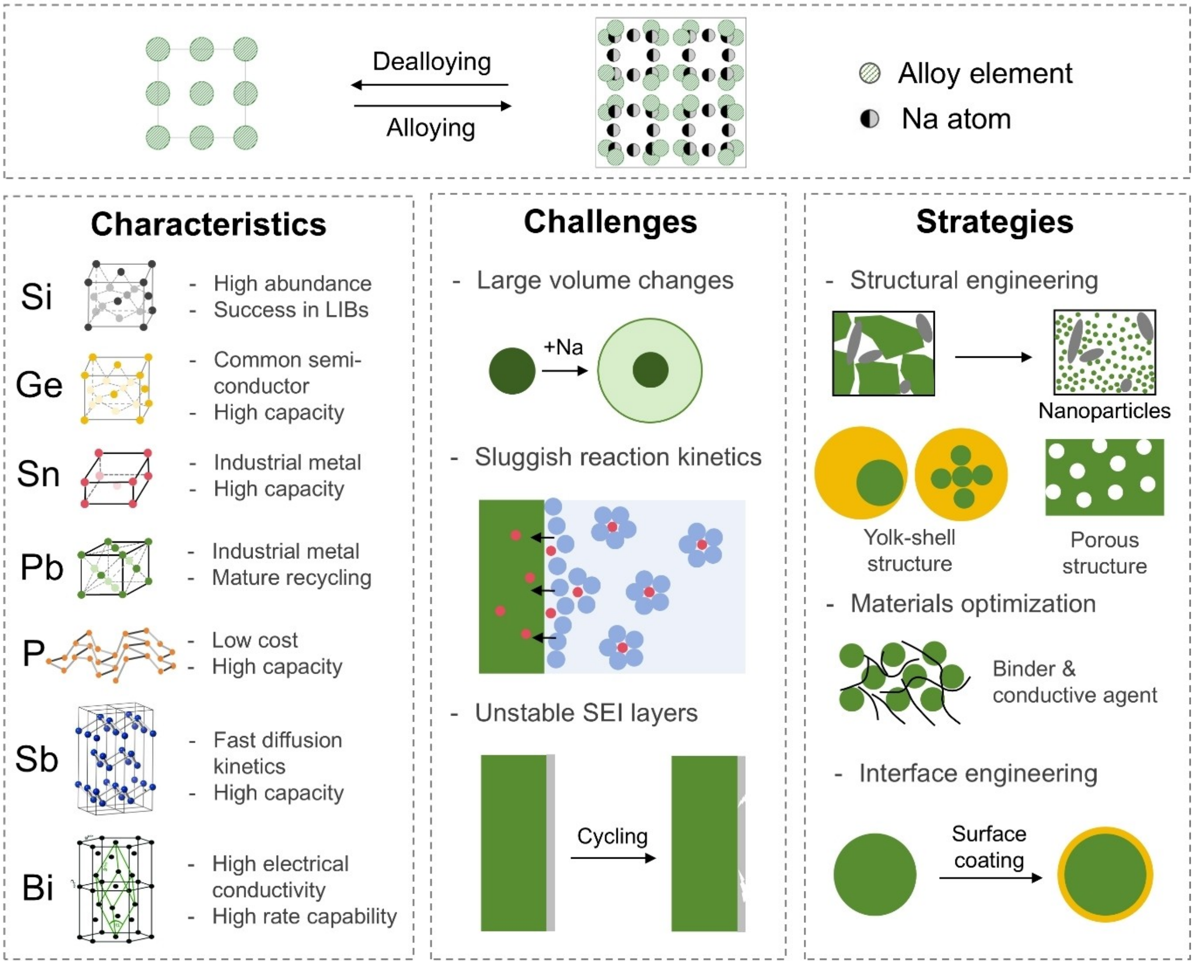

Figure 3. Characteristics, challenges, and strategies for improvements of some typical alloy anodes in SIBs.

of all these elements based on the atomic ratios of the existing intermetallic compounds with the highest Na content. On one hand, the calculated gravimetric values are summarized in Figure 4a to set a baseline reference for potential SIB anode candidates. On the other hand, volumetric capacities for alloy anodes may not be as essential since Na incorporation will occupy roughly 23.75 cm^3 mol^{-1}, regardless of the alloy hosts. Chevrier and Ceder have drawn the universal volume expansion curve of Na-based alloy anodes and compared it with Li-based ones (Figure 4b), from which the volumetric energy density is only affected by the equilibrium potentials of these alloy anode candidates.[21] Therefore, the gravimetric capacity of these alloy anodes alone can partly represent the energy density that can be achieved in full SIB cells. When the volumetric energy density is considered the only criterion, SIBs can hardly be competitive with LIBs because the volume expansion induced by Na incorporation is approximately 2–3 times greater than that resulting from the incorporation of an equivalent number of Li atoms. Figure 4b highlights that Na alloy anodes exhibit significantly lower volumetric energy densities at the same degree of volume expansion.

Pb-acid batteries (PABs) may be a more appropriate candidate to be compared with SIBs. In 2018, around 70 % of the global energy storage market was occupied by PABs, with a revenue of 80 billion USD and a total production of 600 GWh.[22] Although lead is toxic, the well-established and economic recycling processes make it distinctive, explaining why PABs are the second most adopted battery products in modern life. Currently, the recycling of PABs is nearly a closed-loop process with more than 99 % of lead-containing materials being recovered. While the process relies on conventional pyrometallurgy methods, the emissions are strictly controlled to minimize negative environmental impacts.[23] Compared to PABs, SIBs offer advantages in prolonged cycling life and enhanced rate capability. Specifically, SIBs can achieve ~5000 cycles and operate at a rate of ~5 C, whereas PABs typically sustain fewer than 1000 cycles and a maximum rate of 1 C. These performance characteristics make SIBs promising for the automotive industry and stationary applications as complementary energy storage solutions.

3. Group IVA Elements as Anodes in Sodium-Ion Batteries

The alloy elements in Group IVA seem to hold great potential to be promising candidates for SIB application as opposed to those in other chemical groups. For instance, gallium will melt when the temperature is beyond ~30 °C and therefore can hardly handle common battery working conditions. The abundances of indium, antimony, bismuth, and selenium are not particularly higher than that of the precious metal (silver), while tellurium is one of the rarest metals on Earth. Thallium and arsenic are extremely toxic and have been strictly controlled in many countries. In Group IVA, various carbon materials are commercially available, including graphite for LIBs and HC for SIBs. Silicon (Si) and Germanium (Ge) are common materials in the semiconductor industry while both Tin (Sn) and Lead (Pb) are major industrial metals.

Before moving into each alloy element independently, their material properties are provided in Table 1 to shed light on the similarities and differences within SIB systems. The same crystal structure (i.e., diamond face-centered cubic; FCC) of Si and Ge should be acknowledged, of which the latter has a slightly larger lattice constant (0.543 nm vs. 0.566 nm). They have similar electronic structures with the same valence electron configurations ($3s^2p^2$ for Si vs. $4s^2p^2$ for Ge).[24] The mechanical moduli are also similar for both elements, giving them a generally brittle nature. The only notable difference may be that the electric conductivity of Ge (2.17 S cm^{-1}) is about 4 orders of magnitude higher than that of Si (4.35×10^{-4} S cm^{-1}). Concerning Sn and Pb, they are common industrial metals with similar mechanical properties and electrical conductivities. The difference between them lies in the crystalline structures: The former has a tetragonal structure, while the latter has an FCC

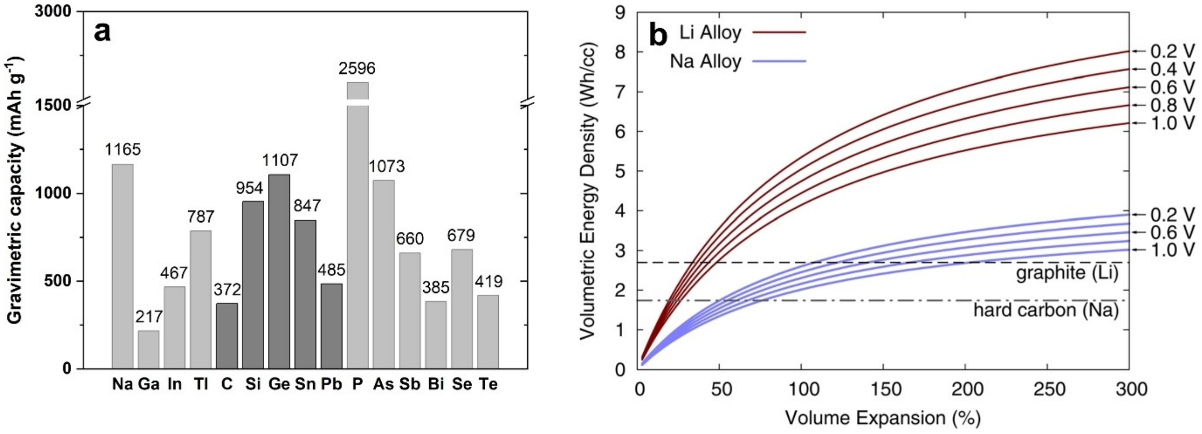

Figure 4. (a) Calculated gravimetric capacities of various alloy anode candidates considering the formation of the highest sodiated compounds. (b) Universal expansion curves for Li and Na alloys. The volumetric energy densities of lithiated graphite and sodiated hard carbon are included for ease of comparison but are not a function of the volume expansion axis. Reprinted with permission 2011 The Electrochemical Society, IOP Publishing, Ltd.[21]

Table 1. Comparisons of the physio-chemical properties of Si, Ge, Sn, and Pb anodes. The data are obtained from Ref. [25b,27].

Element	Crystal structure	Lattice parameters			Bond length/nm	Mechanical moduli/GPa			*B*/*G* ratio	Electrical conductivity at 293 K/S cm^{-1}
		a/nm	b/nm	c/nm		Elastic (*E*)	Bulk (*B*)	Shear (*G*)		
Si	Face-centered cubic (diamond)	0.543	0.543	0.543	0.236	164.80	99.20	67.30	1.47 brittle	4.35×10^{-4}
Ge	Face-centered cubic (diamond)	0.566	0.566	0.566	0.246	135.00	76.80	55.90	1.37 brittle	2.17
Sn	Body-centered tetragonal	0.350	0.350	0.468	0.341/ 0.350	51.01	45.00	17.93	2.51 ductile	$\sim9.17\times10^{6}$
Pb	Face-centered cubic	0.492	0.492	0.492	0.353	33.70	38.50	12.20	3.16 ductile	$\sim4.55\times10^{6}$

structure. Compared to Si/Ge, Sn/Pb have much larger lattice parameters and more flexible lattice structures with weak metallic Sn–Sn/Pb–Pb bonds as opposed to the strong covalent Si–Si/Ge–Ge bonds. These features of Sn and Pb can facilitate easier Na diffusion into their structure, enabling faster (de−)sodiation kinetics.[25] Furthermore, while Si and Ge are semiconductors and brittle materials, Sn and Pb are soft and ductile metals. These differences can result in variations in mechanical deformation during the Na (de-)alloying. The plastic deformation probably takes place in the case of Sn and Pb when the stress developed the alloying process is larger than the yielding strength of Sn or Pb matrix.[13a,26] In contrast, rigid Si and Ge have higher yielding strength, and less significant deformation will be induced by the Na incorporation. Given that the matrix properties play critical roles in the Na (de−)alloying behavior, it may be reasonable to pay extra attention to these similarities and differences when interpreting electrochemical data from Na-based systems using these elements as electrodes.

3.1. Na-M$_{IVA}$ Binary Phase Diagrams

Figure 5 displays the documented phase diagrams of Na-M$_{IVA}$ (M$_{IVA}$ = Si, Ge, Sn, Pb) systems, providing the theoretical basis for the sodiation of the M$_{IVA}$ elements. As shown in Figure 5a, there are two intermetallic phases (i.e., Na_4Si_{23} and NaSi) described in the Na–Si phase diagram, which was drawn based on partial solubility data and (non−)stoichiometric phase data.[28] In Figure 5b, three intermetallic phases are reported in the Na–Ge phase diagram, namely $NaGe_4$, NaGe, and Na_3Ge.[29] The Na–Sn phase diagram (Figure 5c) indicates the presence of eight Na–Sn intermetallic phases, i.e., $NaSn_6$, $NaSn_4$, $NaSn_3$, $NaSn_2$, NaSn, Na_9Sn_4, Na_3Sn, and $Na_{15}Sn_4$, with their formation energy estimated by Choi et al. based on the first principle calculations.[30] The Na–Pb phase diagram (Figure 5d) describes five Na–Pb intermetallic compounds, i.e., β-phase, NaPb, Na_5Pb_2, Na_9Pb_4, and $Na_{15}Pb_4$ that may form during the Na alloying of Pb. It should be noted that there are two single-phase regions, one corresponding to the β phase with a Na content range of ca. 28–35 at%, and the other corresponding to $Na_{15}Pb_4$ with a narrower Na content range of ca. 79–80 at%. Overall, it is noted that some of the mentioned Na-M$_{IVA}$ intermetallic compounds are never observed electrochemically but are reported to exist either by density function theory (DFT) calculations or metallurgical melting/mixing procedures. While the underlying mechanisms remain unclear, the high energy barriers for nucleating certain sodiated crystalline phases are suggested to be partly responsible for these inconsistencies.[31]

3.2. Electrochemistry and Phase Transformations

3.2.1. Na-Si System

Si was perhaps at the top of the agenda when people started extending Li-based electrochemistry to Na-based one owing to its emerging success in LIBs and mature supply chain.[20] The Na–Si phase diagram in Figure 5a was established based on the data harvested from a metallurgic mixing-heating approach at 700 °C through X-ray diffraction (XRD) tests,[28a] which may not fully reflect the electrochemical behavior of the Na–Si system at room temperature. Based on the DFT calculations of total energy (dashed line in Figure 6a), the NaSi phase should be formed electrochemically and thermodynamically stable at an electrode potential slightly above 0 V vs. Na/Na$^+$, agreeing with the phase diagram.[21] Inconsistently, however, the electrochemical sodiation of Si at room temperature has not been observed experimentally to date.

Numerous attempts have been made to facilitate the electrochemical alloy of Na and Si but with limited success. For instance, Ellis et al. increased the test temperature to 60 °C, aiming to unlock the sodiation of **Si thin film** electrodes through enhanced diffusion kinetics but neither reversible capacity nor change in XRD results was observed.[34] Zhang et al. recently repeated the electrochemical tests at 65 °C by running several dummy cells to rule out the effects from the surface reactions and suggest that Si thin films seem electrochemically inactive to Na at this moderate temperature regime (inset of Figure 6a),[27] agreeing with Komaba et al. as well.[35]

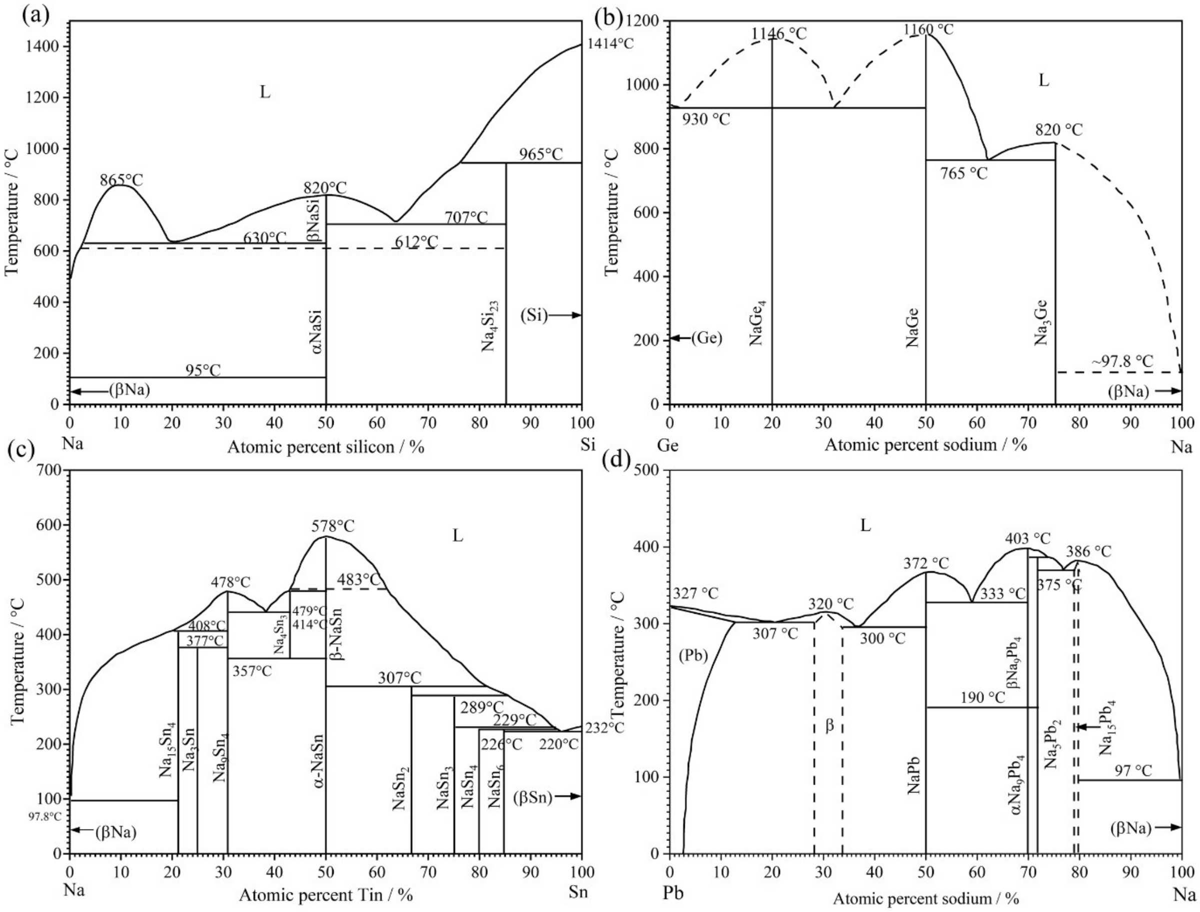

Figure 5. (a) The Na–Si binary phase diagram with the data collected from Sangster and Pelton.[28a] (b) The Na–Ge binary phase diagram with the data collected from Sangster and Pelton.[29] (c) The redrawn Na–Sn binary phase diagram.[32] (d) The redrawn Na–Pb binary phase diagram.[33]

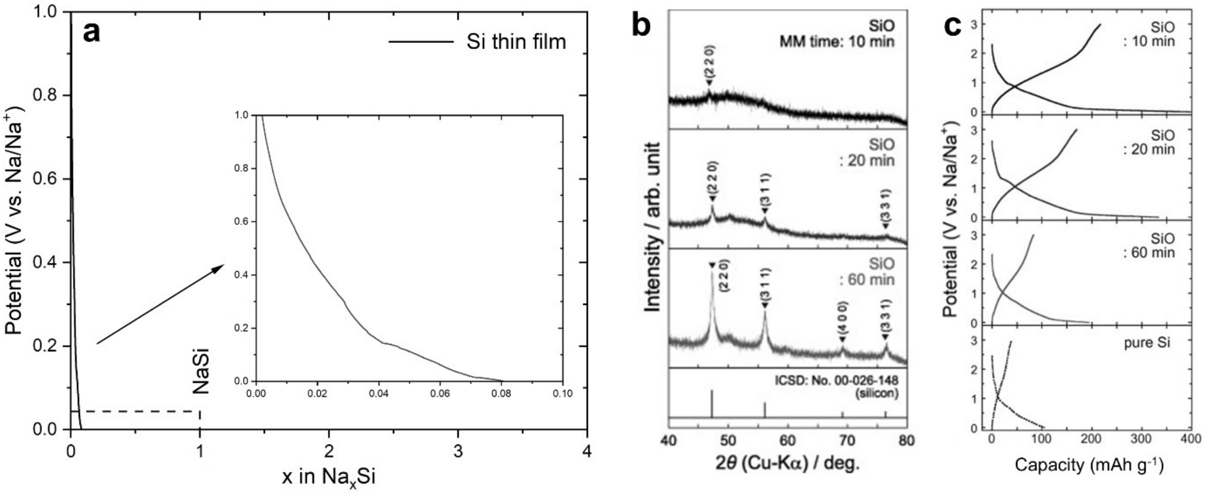

Figure 6. (a) Experimental (solid line)[27] and calculated (dashed line)[21] voltage curves of the initial sodiation of the Si electrode. (b) X-ray diffractograms and (c) galvanostatic charge-discharge profiles of the SiO powders prepared by mechanical milling for 10 min, 20 min, and 60 min. Adapted with permission 2015 Elsevier B.V.[36]

Differently, a Japanese group did observe a desodiation capacity of ~90 mAh g^{-1} from an amorphous **Si composite** electrode at 80 °C,[36] but the value is far away from the calculated one, i.e., 725 mAh g^{-1}.[37] In other words, the predicted Na–Si intermetallic compounds can hardly be formed electrochemically, e.g., $Na_{0.76}Si$ and $Na_{0.75}Si$.[37–38] The authors, however, realized that the Si atoms within the SiO_4 matrix seem to become electrochemically active to Na, absorbing Na atoms to form Na–Si binary alloy (Figure 6b). This SiO_4 electrode is prepared by 10-minute ball-milling of SiO, which gives desodiation capacity of ~220 $mAh\,g^{-1}$ in the initial cycle (Figure 6c).[36] Also, when Si is mixed with MXene to fabricate an electrode with densely packed Si/MXene microspheres, a possible formation of the $NaSi_6$ phase is reported.[39]

At the end of the day, the unsatisfied Na storage behavior of the Si anode observed experimentally may be explained by the following factors: (1) The sluggish diffusion of Na in Si; (2) the poor electrical conductivity of Si; (3) the weak atomic force between Na and Si.[37] It is suggested by Zhang et al. that alternative ways of exploration are required to understand why the electrochemical sodiation of Si is often inert.[27]

3.2.2. Na-Ge System

As briefly mentioned, the crystal and electronic structure of Ge is very similar to that of Si but with a slightly larger lattice constant.[40] The looser and more flexible crystal lattice may be beneficial for nucleation and growth of new (lithiated/sodiatied) phases in alloy electrodes.[41] A DFT study calculated that the energy barrier of migration of interstitial Na in Ge (0.78 eV) is lower than that in Si (1.08 eV), leading to more favorable Na transportation in both the Ge and the Na–Ge phases.[25a] Consistently, Ge with a low degree of crystallinity is found to be electrochemically active to Na.[42] However, the phase diagram, the DFT calculations, and the electrochemical data do not seem to agree with each other. The DFT calculations (dashed line in Figure 7a) suggest that the three most thermodynamically stable phases should be $NaGe_2$, NaGe, and $Na_{1.5}Ge$,[38] rather than $NaGe_4$, NaGe, and Na_3Ge described in the phase diagram (Figure 5b). While a few studies reported the sodiation capacity of 369 $mAh\,g^{-1}$, agreeing nicely with the formation of the NaGe phase,[43] the final sodiated Na–Ge phase in most experimental studies often gives a Na : Ge ratio beyond the ideal 1 : 1, such as $Na_{1.16}Ge$,[42] $Na_{1.4}Ge$,[44] and $Na_{1.6}Ge$,[18] closer to the calculated $Na_{1.5}Ge$ phase.

Recently, Zhang et al. conducted systematic electrochemical investigations on **Ge thin film** electrodes and attributed this stoichiometric variation to being largely controlled by diffusion kinetics. They tried to sodiate a Ge thin film electrode extraordinarily slowly (i.e., C/100) and obtained a final stoichiometry is $Na_{1.38}Ge$ at room temperature (Figure 7b). Slightly elevated temperatures are found to facilitate the Na incorporation, forming $Na_{1.41}Ge$ at 40 °C, $Na_{1.59}Ge$ at 50 °C, and $Na_{2.3}Ge$ at 60 °C (Figure 7c-e).[27] It is worth noting that the formation of the Na-poor phase, possibly $NaGe_4$, is significantly affected by the sodiation temperature, indicated by the shift of the reduction peak in the corresponding *dQ/dV* curves, i.e., arrows in Figure 7c-e. This first phase transformation (i.e., possible formation of $NaGe_4$) does not seem reversible as its electrochemical features disappear after the initial sodiation. Another noteworthy feature is that the desodiation peak at 60 °C splits,

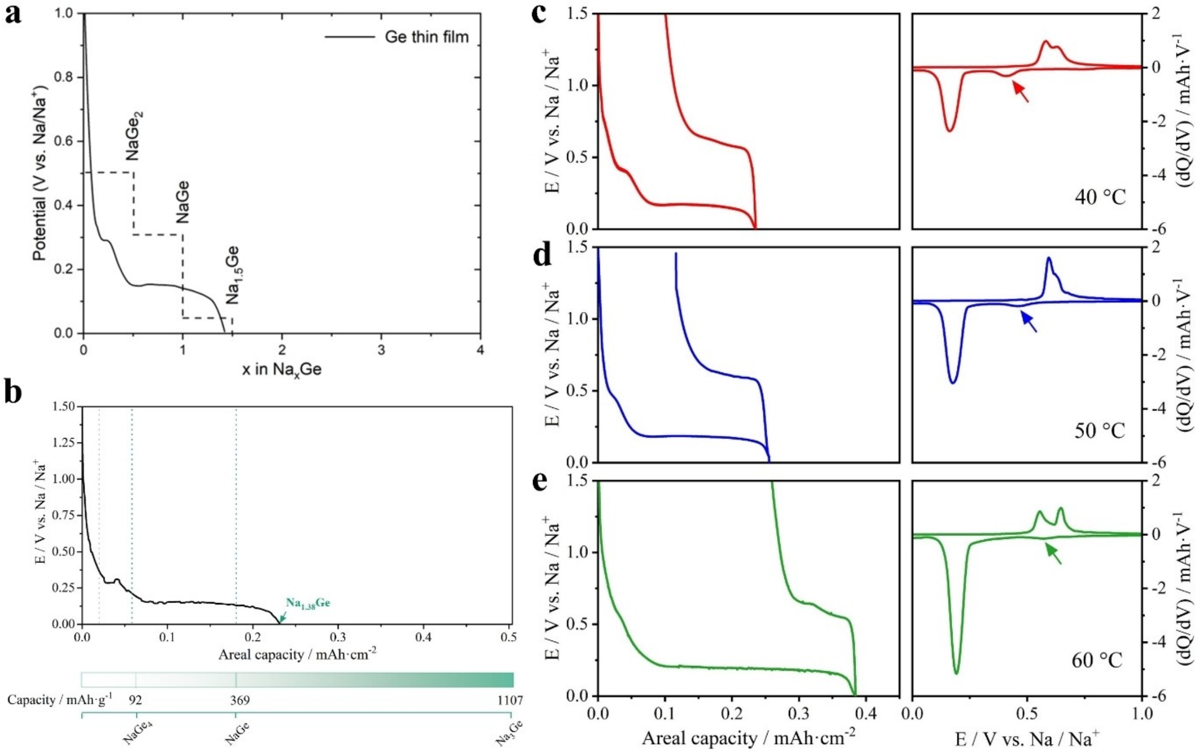

Figure 7. (a) Experimental (solid line)[27] and calculated (dashed line)[38] voltage curves of the initial sodiation of the Ge electrode. (b) The potential vs. areal capacity profile of Ge electrodes in the first sodiation process, with the capacity quantification shown in the bottom green lines. The potential vs areal capacity profiles of Ge electrodes conducted at 1/100 C and its corresponding dQ/dV at elevated temperatures, (c) 40 °C, (d) 50 °C, and (e) 60 °C. Adapted 2023 CC BY 4.0.[27]

originating from the two desodiation plateaus in the GCD profile (Figure 7e). The authors suggested that a Na-rich phase, likely Na_3Ge in addition to NaGe, is forming at slightly elevated temperatures due to enhanced reaction kinetics but necessitates further investigations due to the amorphous nature of the Na–Ge phases, which cannot be characterized by regular XRD techniques.[27] It is not uncommon that reaction kinetics affect the final phase formation in some alloy anodes, such as the formation of $Li_{22}Si_5$[45] and $Li_{2-x}Al$ in LIBs,[46] which can only be observed under kinetically favorable conditions. Lastly, one can tell from the evident irreversible capacity that the electrode reversibility of Ge thin films is poor, resulting in unsatisfied cycling performances of only a few cycles.

To summarize, limited literature is available regarding how Ge functions as an anode in SIBs but this section covers some key information: (1) The final product of Ge upon full electrochemical sodiation is unlikely the NaGe phase; (2) the formation of Na–Ge phases beyond 1:1 atomic ratio is kinetically-limited; (3) the Na–Ge phases formed electrochemically seem to be present in amorphous states, which warrant further verification.

3.2.3. Na-Sn System

The dashed line in Figure 8a presents the galvanostatic profile calculated from existing crystal structures using DFT, which highlights four Na–Sn intermetallic phases.[21] While the experimental data seems to agree with the calculations, the sodiation potential plateaus of Sn thin film electrodes are generally lower than the calculated ones.[47] In addition to thin films, the galvanostatic profile of Sn foil is also included in Figure 8a, which only exhibits three potential plateaus. The explorations of the reaction mechanisms of Sn anodes reveal that, except for the final sodiated phase $Na_{15}Sn_4$, the intermediate Na–Sn phases formed during the sodiation do not precisely match the ones described in the phase diagram (Figure 5c).

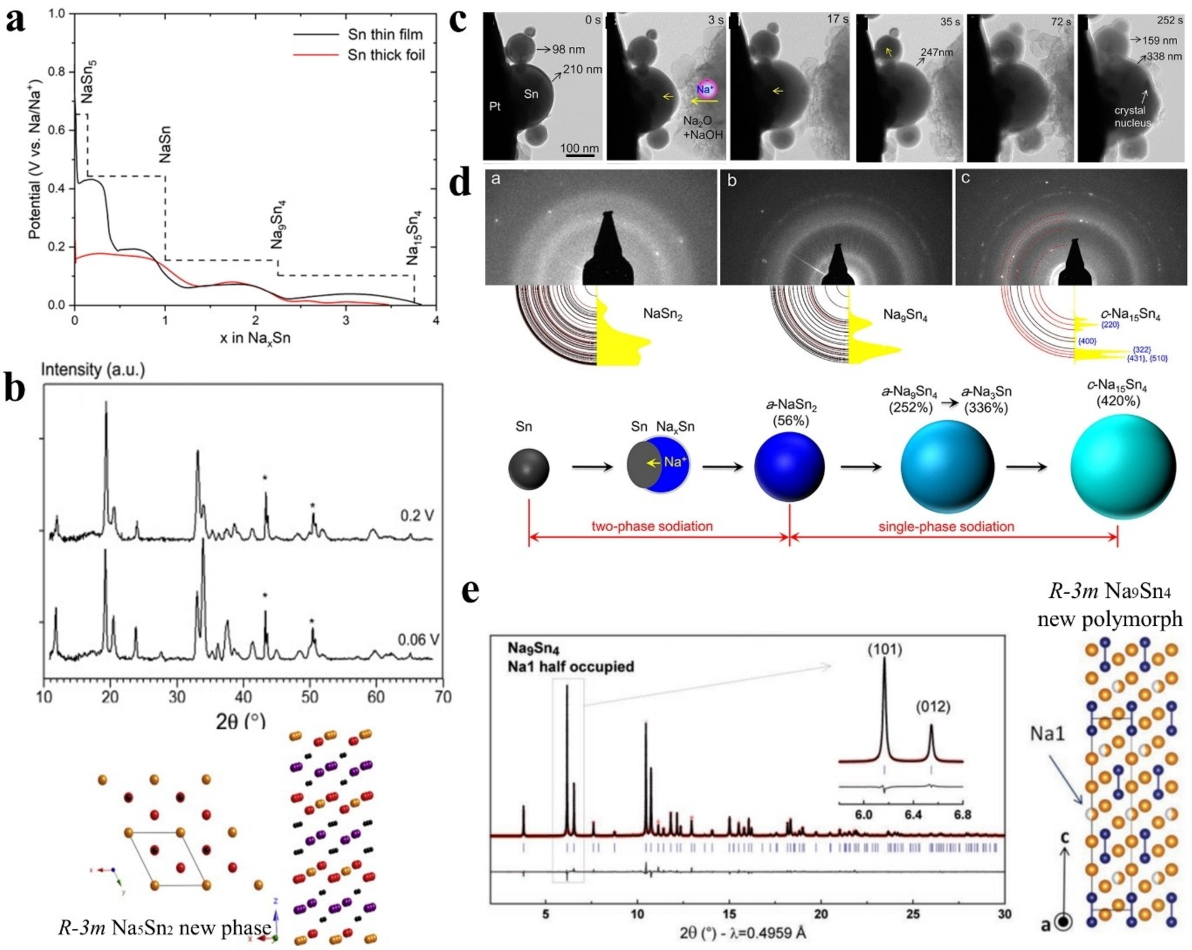

Figure 8. (a) Experimental (solid lines)[47] and calculated (dashed line)[21] voltage curves of the initial sodiation of Sn film (2 μm) and foil (30 μm) electrodes. (b) X-ray diffractograms of the Sn electrode sodiated until 0.06 V and desodiated to 0.2 V, corresponding to the hexagonal *R-3 m* phase of nominal composition Na_5Sn_2 and electrochemical composition of $Na_{2.4}Sn$. (*) indicates the diffraction peaks contributed by the Cu current collector. Adapted with permission 2013 Elsevier B.V.[51] (c) The morphological change (TEM images) of Sn nanoparticles during the initial sodiation. (d) The diffraction pattern of the sodiated phases, and the schematic illustration showing the structural change of Sn during the sodiation. Adapted with permission 2012 American Chemical Society.[52] (e) The experimental synchrotron X-ray diffractogram (red line) of Na_9Sn_4, which agrees with the calculated one (black one), with a small difference between them (bottom gray line). Adapted with permission 2016 John Wiley and Sons.[53]

In the case of **Sn thin film** electrodes, Ellis et al. investigated their electrochemical sodiation behavior at a rate of C/50 at ambient temperature. The galvanostatic sodiation profile of Sn film is characterized by four different potential plateaus, analogous to the one presented in Figure 8a. Through in-situ XRD measurements, it is found that a deep sodiation of the Sn film electrode to 5 mV vs. Na/Na^+ gives an X-ray diffractogram that is indicative of the crystalline $Na_{15}Sn_4$ phase. However, in the case of partly sodiated Sn film, the diffractograms obtained at the end of each potential plateau do not agree with the documented Na–Sn intermetallic phases. As determined by the coulometry method, one of the intermediate phases is amorphous with a similar stoichiometry of NaSn, while the other two are crystalline with compositions close to $NaSn_3$ and Na_9Sn_4, respectively.[48] Noteworthy, Yamamoto et al., in the exploration of the thermodynamic behavior of Sn thin films during sodiation at 90 °C, reported the formation of a crystalline NaSn phase.[49] This finding of the NaSn formation at elevated temperatures indicates that poor kinetics or high nucleation barriers can be the limiting factors for the formation of crystalline intermediate Na–Sn phases. Baggetto et al. examined the sequence of the intermetallic Na–Sn phases formed during the sodiation of a 2 μm-thick Sn thin film at room temperature.[43] The major crystalline peaks of the X-ray diffractogram, after the first sodiation plateau, do not agree with any documented Na–Sn intermetallic phases, suggesting the formation of a new phase with an undetermined crystal structure. Cluster-expansion-based structure predictions indicate that this new crystalline phase has a similar stoichiometry of $Na_{0.6}Sn$. By the end of the second sodiation plateau, an amorphous phase is likely formed at the composition close to $Na_{1.2}Sn$. Moreover, a metastable hexagonal *R-3m* Na_5Sn_2 phase (Figure 8b) was also detected by XRD in the initial sodiation of 100 nm Sn thin film electrodes but was largely suppressed upon the cycling. After the full sodiation, a crystalline *I-43d* $Na_{15}Sn_4$ phase was formed, as supported by a fit between the X-ray diffractogram of the Sn film electrode and the standard one of $Na_{15}Sn_4$.[47] Continuous efforts by Baggetto et al. were made to elaborate on the formation of Na_xSn ($x > 1$) in Sn thin film electrodes, which generates more insights into the mechanisms of the Na–Sn system: A thermodynamically stable *R-3m* Na_7Sn_3 phase instead of Na_5Sn_2 is formed in the electrochemical sodiation of Sn film at room temperature. Furthermore, it is found that Na_9Sn_4 does not readily form at 175 °C and its formation seems to only occur close to or above the melting temperature.[50]

The electrochemical behavior of the 30 μm-thick **Sn foil** electrode shown in Figure 8a is found to be inconsistent with that of Sn thin films but agrees with other Sn foil works. Du et al. observed three sodiation potential plateaus (instead of four for thin films), which are suggested to result from the unfavorable electrode kinetics of bulk Sn foils.[51] This claim was well supported by Baggetto et al. who varied the thicknesses of Sn film electrodes and found that the kinetical behavior becomes worse as the electrode thickness increases, leading to the merging of sodiation potential plateaus.[47] Ex-situ XRD characterization shows that after the first plateau, the XRD peaks agree well with the crystalline NaSn (1:1) phase, which was also reported as α-NaSn in an earlier study.[54] But in 1999, Grin et al. determined the crystal structure of a Na–Sn phase with a 1-to-1 atomic ratio, which was denoted as Na_4Sn_4.[55] In previous works, the NaSn phase with an amorphous or nanocrystalline nature was also reported as one of the sodiation products of Sn thin film.[47–48] By comparing several broad and low-intensity diffraction peaks with that of Na_4Sn_4 formed in the sodiation of a 30 μm-thick Sn foil electrode, the authors found that these diffraction peaks generally agree with each other. Differently, the diffraction peaks of Na_4Sn_4 formed in the sodiation of Sn foils exhibit higher peak-to-width ratios, indicative of stronger crystallinity. The authors hence suspected that the suppression of NaSn crystallization in the sodiation of the Sn thin film electrode could be associated with the misfit strain between the Sn electrode and the Cu substrate. At the end of the second sodiation plateau of the Sn electrode, the X-ray diffractogram of the electrode is found to be indicative of Na_5Sn_2 (Figure 8b), as assigned by Baggetto et al.,[47] rather than the commonly adopted Na_9Sn_4. Additionally, the XRD peaks of the deeply sodiated Sn foil are in line with that of the $Na_{15}Sn_4$ phase, which confirmed $Na_{15}Sn_4$ as the final sodiation product of Sn foil electrodes.[51] In 2021, Kim et al. revisited the phase transitions of Sn foil electrodes during electrochemical (de–)sodiation at C/100 using in-situ XRD and suggested that the sodiation occurred through the formation of Na_xSn ($x < 1$), β-NaSn, Na_9Sn_4, and $Na_{15}Sn_4$.[56]

For **Sn composite** electrodes, Komaba et al., based on XRD analyses, suggested that a full sodiation covers the formation of $Na_{15}Sn_4$, with $NaSn_5$, NaSn, and Na_9Sn_4 as the intermediate phases, which leads to the appearance of four distinct plateaus in the galvanostatic profiles.[35,57] On the contrary, a subsequent in-situ TEM study by Wang et al. revealed a different sodiation mechanism.[52] Figure 8c illustrates the microstructure change of the Sn (nano–)particles during the sodiation. At the early stage of sodiation, Na atoms are inserted into the Sn nanoparticles and move the phase boundary, but no clear phase boundary can be observed when sodiation becomes deeper.[52] Combining with the electron diffraction patterns, the authors thereby proposed that the sodiation of Sn nanoparticles initially proceeds through a two-phase mechanism with a moving phase boundary to form an amorphous $NaSn_2$ phase, and subsequently occurs via a single-phase mechanism to form the amorphous Na_9Sn_4, amorphous Na_3Sn phase, and crystalline $Na_{15}Sn_4$ phase successively (Figure 8d).[52] Zhang et al. also investigated the phase transformations of the microsized Sn particles, where it is found that the electrochemical behaviors in ether-based electrolytes are similar to those in carbonate-based electrolytes reported in previous works, with galvanostatic profiles all featured by four potential plateaus.[53] The XRD results of the electrochemically sodiated Sn composite electrodes to 0.11 V vs. Na/Na^+ after annealing at 100 °C for 24 h were indexed to be consistent with the crystalline NaSn phase prepared by ball-milling. Also, the X-ray diffractogram obtained from the Na/Sn mixture that underwent the ball-milling process with an atomic ratio of 2.25 (i.e., Na_9Sn_4) matches that of the Sn composite electrode after the sodiation to 0.05 V vs. Na/Na^+.

The authors thus postulated the NaSn and Na_9Sn_4 as the electrochemical sodiation products of Sn composite electrodes.[53] However, the diffractogram of this synthesized Na_9Sn_4 is found to be different from the one with the same composition which has the space group of *Cmcm* reported previously, indicating a new polymorph Na_9Sn_4 phase.[53] Through in-depth structural analyses, the authors identified that the new polymorph Na_9Sn_4 crystallizes in the space group *R-3m* and has a crystal structure of rhombohedral (Figure 8e).[53]

Recently, an in-situ hard X-ray nano-tomography study demonstrated that the sodiation of Sn composite electrodes progresses by the formation of Na_xSn ($x \approx 1.3$), and then the formation of Na_9Sn_4 or higher-order Na_xSn ($x > 2.25$) phases.[58] Stratford et al. proposed a new reaction mechanism for the Na–Sn system based on the solid-state nuclear magnetic resonance (NMR) analysis combined with theoretical calculations: Sn composite electrodes are first sodiated to form a crystalline layer-structured Na–Sn phase with the Na : Sn ratio of approximately 1 : 3 (i.e., $NaSn_3$ as an intermediate), followed by a transition to a thermodynamically stable crystalline phase $NaSn_2$ with the same crystal structure.[59] Further sodiation can result in the formation of amorphous $Na_{1.2}Sn$. The authors then reported a solid-solution transition from the a-$Na_{1.2}Sn$ to crystalline $Na_{5-x}Sn_2$ and $Na_{15}Sn_4$, and that additional Na can be inserted into $Na_{15}Sn_4$ to form a $Na_{15+x}Sn_4$ compound in a process similar to the documented transformation from crystalline $Li_{15}Si_4$ to off-stoichiometry phase $Li_{15+x}Si_4$ at higher lithiation depth.[59–60]

To summarize, quite a few works have been carried out to study Sn-based electrodes in SIB systems and we highlight some key information here: (a) Electrochemical behavior is affected by the electrode architectures, i.e., thin films, thick foils, and composites; (b) while $Na_{15}Sn_4$ is generally considered the final sodiation compound, the formation and nature of intermediate Na–Sn phases remain debatable; (3) whether these intermediate phases are (partly) amorphous or crystalline requires further verification. Since amorphous materials lack long-range periodicity, standard Bragg diffraction is ineffective, sychrotron high-energy X-ray techniques are preferred to help answer the remaining questions, such as synchrotron-based X-ray total scattering or X-ray absorption spectroscopy.

3.2.4. Na-Pb System

Though the perceived toxicity may result in human health risks and environmental concerns, Pb is one of the most recycled metals owing to its well-established recycling processes. Together with high volumetric capacity (~1175 $mAh\,cm^{-3}$), cost-effectiveness (~2 $USD\,kg^{-1}$ or ~0.5 $USD\,mol^{-1}$),[61] and decent electric conductivity, Pb should be a promising candidate for the low-cost and high-capacity anode in SIBs, especially considering its success in PABs. In general, inconsistencies remain between the Na–Pb phase diagram and the DFT calculations or experimental data, where neither the β phase nor its homogeneity range described in Figure 5d is observed. The inaccurate measurement of homogeneity range at room temperature was also observed in other binary alloys, e.g., Li-Al system.[62a] As shown in Figure 9a, other than the Na_5Pb_2 phase, which was intentionally excluded from the DFT calculations, the remaining phases agree quite nicely with the experimental data of the Pb thin film electrode.[21] Pb thick foil, differently, only exhibits three distinct plateaus at lower potentials vs. Na/Na^+ but the overall specific capacity matches that obtained from the Pb thin film, perhaps due to different kinetic behaviors of films and foils.[62b] The galvanostatic profile of Pb composite electrode generally agrees with that of Pb thin film and therefore is not included in Figure 9a. Recently, Garayt et al. established a correlation between the normalized unit cell volume and the atomic ratio of each Na–Pb phase,[63] highlighting intermetallic Na–Pb phases formed during sodiation (Figure 9b).

Ellis et al. conducted an in-situ XRD examination on the sputtered **Pb thin film** electrode and investigated the intermetallic phases formed during sodiation.[34] The X-ray diffractograms shown in Figure 9c indicate that the four potential plateaus of the Pb thin film electrode correspond to the four Na–Pb phases, namely $NaPb_3$, NaPb, Na_9Pb_4, and $Na_{15}Pb_4$. The Pb thin film electrode delivers a specific capacity of 484 $mAh\,g^{-1}$, which perfectly matches the one calculated from the formation of the $Na_{15}Pb_4$ phase. During the sodiation, it is concluded that the α-Na_9Pb_4 phase, which has the same crystal structure as that of Na_9Sn_4, is formed at the end of the 3rd potential plateau.[34]

Zhang et al. conducted an ex-situ XRD study on the electrochemical sodiation of 30 μm **Pb foil** electrodes.[64] It is suggested that different from the previously discussed Pb thin film electrode, the phase transformations during the initial sodiation of Pb foil electrodes are probably occurring simultaneously rather than sequentially, which largely explains merely three sodiation plateaus in the initial cycle (Figure 9a). The simultaneous formation of multiple Na–Pb phases is supported by a series of X-ray diffractograms in Figure 9d. A full sodiation of the Pb foil electrode gives a specific capacity of ~460 $mAh\,g^{-1}$, agreeing with that of the Pb film electrode. The difference in electrochemical behavior between Pb thin films and Pb thick foils is believed to originate from the poor Na transportation in bulk (Na—)Pb phases and the localized mechanical stresses caused by volume expansion.[64]

More studies can be found on **Pb composite electrodes**, which follow a commercial electrode design. In general, the electrochemical behaviors of Pb composite electrodes largely replicate those of a Pb thin film, yielding four distinct potential plateaus with an initial sodiation capacity of 480 $mAh\,g^{-1}$.[35] In 1987, Jow et al. demonstrated a dealloying process of the $Na_{15}Pb_4$ composite electrode prepared by a melting-mixing method.[65] Although the Na_5Sn_2 phase was suggested to form at the end of the 3rd plateau, later it was found to be incorrect by Ellis et al. in 2014.[34] This finding was subsequently confirmed by Darwiche et al.'s work, where the in-situ XRD analysis (Figure 9e) indicates the formation of $NaPb_3$, NaPb, Na_9Pb_4, and $Na_{15}Pb_4$ during the (de—)sodiation process of the Pb composite electrode.[66]

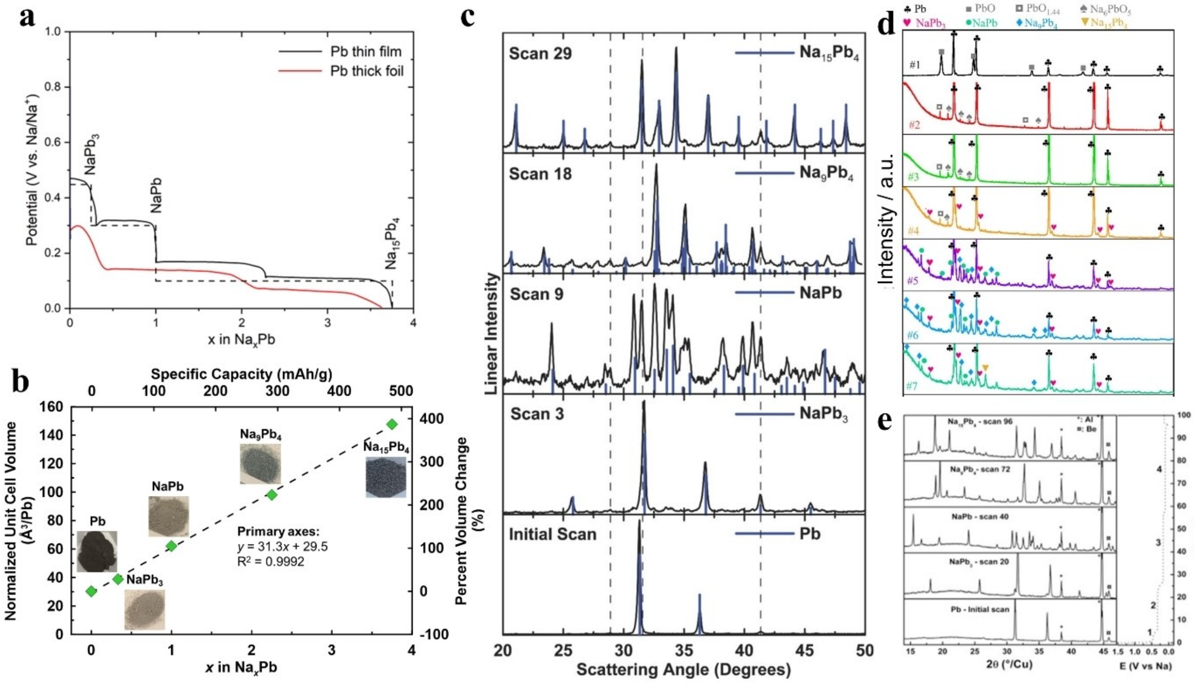

Figure 9. (a) Experimental (solid lines)[34] and calculated (dashed line)[21] voltage curves of the initial sodiation of Pb film and foil electrodes. (b) Normalized unit cell volume of different Na–Pb intermetallic phases (Reprinted 2024 CC BY 4.0).[63] (c) In-situ XRD patterns of different phases formed during the first discharge of a Pb composite electrode versus Na/Na^+ at the end of each voltage plateau. Long dashed lines extending vertically across the figure indicate the position of peaks arising from the in-situ cell parts. Reprinted CC BY 4.0.[34] (d) Ex-situ X-ray diffractograms of Pb foil electrode vs. Na during electrochemical sodiation. Adapted 2014 CC BY 4.0.[64] (e) In-situ X-ray diffractograms of Pb composite electrode vs. Na after each sodiation plateau, which corresponds to the $NaPb_3$, NaPb, Na_9Pb_4, and $Na_{15}Pb_4$ phases, respectively. It is noted that peaks with the labels * and ¤ indicate those of Al current collector and Beryllium window. Reprinted with permission 2015 Elsevier B.V.[66])

After reviewing these Pb works, some key findings need to be acknowledged: (1) The homogeneity range of the β phase shown in the phase diagram (Figure 5d) is never experimentally observed during electrochemical sodiation of Pb at ambient temperatures. (2) The formation of Na_9Pb_4 instead of Na_5Pb_2 is confirmed by the XRD data. (3) Pb thick foil seems to behave differently than its thin film or composite counterparts due to kinetical limitations along the z-axis and localized mechanical stresses.

3.3. Mechanics of Na-M_{IVA} System

Like Li-based systems, Na insertion/extraction into/from alloy anodes will cause volume expansion/contraction, accompanied by phase transformations. As these intermetallic phases have different crystal structures, lattice parameters, molar volumes, elastic properties, etc., a mismatch exists between the pristine matrix and the new phase during the phase transformation, which often leads to the development of mechanical stress at the interface[67] and induce physical damage, such as fracture, disintegration, and loss of electrical contact.[67b,68] In turn, fresh electrode surfaces are exposed to the liquid electrolyte, leading to irreversible consumption of electrolyte salts and solvents over cycling, e.g., secondary SEI formation and gas evolution.[69] Meanwhile, the loss of electric contact between the current collector and the electrode can lead to isolations of Na, which is well-documented in Li-based systems, referring to 'dead Li'.[13b,67–68]

From a thermodynamic perspective, the mechanical stress could cause a decrease in the total Gibb's free energy,[70] giving a lower and/or a higher equilibrium potential during alloying and/or dealloying, respectively (i.e., larger overpotentials).[71] A stress-potential coupling study reported that compressive stresses can shift the lithiation potential of Si thin film electrodes,[12] which should also apply to a similar Na-based system. The mechanical stress-induced potential shifts may be explained by several factors, including a higher nucleation barrier,[12,72] and a change in electronic structure caused by lattice distortion.[30,73] In consequence, these effects resulting from mechanical stress can lead to energy loss during electrochemical cycling, causing capacity degradation.[67a]

In a word, the mechanical behaviors of electrode materials play a significant role in battery performance and degradation. In this part, we primarily review the mechanics of group IVA alloy anodes, and the interplay between mechanical behavior and battery performance: (1) volume change, structure evolution, and mechanical stress induced by (de−)sodiation; (2) mechanical properties of the intermetallic phases; (3) electrode stability during electrochemical cycling.

3.3.1. Na-Si System

Given that the electrochemical sodiation of Si is absent, a theoretical volume change of ~144% (Table 2) is estimated considering the phase transformation from Si to NaSi occurs.[21,36] A first-principle simulation predicted significant reductions in the elastic, bulk, and shear modulus as the sodiation of Si, with a *B/G* ratio of ~1.55 for the NaSi phase (Table 3).[25b] To the best of the authors' knowledge, no experimental data on the mechanical behavior of Si anodes in SIBs has been reported to date.

3.3.2. Na-Ge System

Volume Change, Structure Evolution, and Mechanical Stress. The investigation and quantification of the volume changes and mechanical stresses during (de−)sodiation often necessitate

Table 2. The theoretically calculated and experimentally measured volume expansions for the formation of Na_xSn phases.

Na-M_{IVA} system	Sodiated phases	Theoretical Volumetric expansion	Experimental Volumetric expansion
Na-Si	NaSi	~144%	N/A
Na-Ge	$NaGe_4$	N/A	N/A
	NaGe	~118%	N/A
	$Na_{1.6}Ge$	~205%[85]	>300%[18]
	Na_3Ge	~348%	N/A
Na-Sn	a-$NaSn_3$	~22%	~100%[80,86]
	a-$NaSn_2$	~56%	54%[52]
	NaSn	~130%	~120%[80]
	a-Na_9Sn_4	~252%	211%,[52] 250%[80,86]
	a-Na_3Sn	~336%	317%[52]
	c-$Na_{15}Sn_4$	~420%	400%,[83] 402%,[52] 430%[80]
Na-Pb	$NaPb_3$	~26%	N/A
	NaPb	~100%	N/A
	Na_9Pb_4	~216%	N/A
	$Na_{15}Pb_4$	~358%	N/A

Note: a- and c- denote 'amorphous' and 'crystalline' respectively.
N/A: Not applicable.

Table 3. Structural information and Mechanical properties of Na–M alloys. The data are based on DFT calculations and obtained from Mortazavi et al.,[25b] except those that are otherwise stated.

System	Intermetallic phase	Crystal structure	Space group	Elastic Modulus (*E*) / GPa	Bulk Modulus (*B*) / GPa	Shear Modulus (*G*) / GPa	*B/G*	Brittleness from experimental synthesis
Na-Si	Si	Cubic	$Fm\bar{3}m$	151.60	90.32	62.12	1.45	Brittle
	NaSi	Monoclinic	C2/c	36.59	22.99	14.82	1.55	N/A
Na-Ge	Ge	Cubic	$Fm\bar{3}m$	109.51	60.62	45.68	1.32	Brittle
	NaGe	Monoclinic	$P12_1/c1$	39.17	16.15	18.25	0.88	N/A
Na-Sn	Sn	Tetragonal	*I4/mmm*	56.13	46.74	21.59	2.17	Malleable
	$NaSn_5$	Tetragonal	$P\overline{42}_1m$	42.10	29.20	16.71	1.74	N/A
	$NaSn_3$	Tetragonal	*I4/mmm*	38.52[80]	34.43[80]	14.61[80]	2.36[80]	N/A
	NaSn	Tetragonal	$I4_1/acd$	25.63	17.27	10.23	1.85	N/A
	Na_9Sn_4	Orthorhombic	*Cmcm*	24.11	18.91	9.38	2.01	N/A
	$Na_{15}Sn_4$	Cubic	$I\overline{43}d$	15.01	13.83	5.69	2.42	N/A
Na-Pb	Pb	Cubic	$Fm\bar{3}m$	35.45	41.68	13.06	3.19	Malleable
	$NaPb_3$	Cubic	*Pm-3m*	23.23	32.94	8.43	3.90	Malleable[63]
	NaPb	Tetragonal	*I41/acd*	24.54	15.04	9.99	1.50	Brittle[63]
	Na_9Pb_4	Orthorhombic	*Cmcm*	N/A	N/A	N/A	N/A	Brittle[63]
	$Na_{15}Pb_4$	Cubic	*I-43d*	17.14	13.14	6.68	1.96	Brittle[63]

N/A: Not applicable.

designated electrode architectures as model systems, such as thin films or nanowires.[13b,62,74]

Rakshit et al. conducted an atomic force microscopy (AFM) scan and a substrate curvature study to quantify the volume change and the mechanical stress, respectively, during the sodiation of a **Ge thin film** electrode.[44] The initial sodiation of the amorphous Ge (α-Ge) film delivers a specific capacity of 534 mAh g^{-1}, equivalent to a $Na_{1.45}Ge$ stoichiometry. The AFM images in Figure 10a indicate that the volume expansion is ~239% at the end of the initial sodiation, generally consistent with the value calculated by Jung et al. upon the formation of $Na_{1.56}Ge$ (205%) if taking into account the SEI thickness.[37] As shown in Figure 10b, the stress data during the initial sodiation, which yields a flat profile, is notably different from the subsequent cycles. The authors have attributed the flat stress profile of the initial sodiation to the diffusion-limited reactions, which separate the Ge film electrode into Na-rich and Na-poor regions and restrict the mechanical stress at the phase boundary.[44] Thereafter, the stress profile becomes repeatable during the first desodiation and subsequent cycles. The Na incorporation or extraction leads to a compressive or tensile stress of roughly ~100 Pa-m.[44] Interestingly, the peak compressive stress in the Ge film caused by sodiation is −0.56 GPa, which is roughly half of that caused by lithiation, i.e., −1.1 GPa.[75] This observation seems contradictory to the general belief that the sodiation could give rise to a larger stress than that of lithiation due to the larger atomic size of Na. But in fact, the Ge network can accommodate significantly more Li than Na for similar volume changes, resulting in a higher stress upon lithiation. In any case, a volume change of ~239% and a compressive stress of ~0.56 GPa upon sodiation is non-trivial and could cause severe physical damage to Ge anodes (e.g., cracking and changing in surface morphology; Figure 10c-d), largely explaining why Ge thin film electrodes do not exhibit satisfactory cyclabilities.[44]

By employing the in-situ TEM technique, Lu et al. observed a more than 300% volume expansion in **Ge nanowires** by the end of initial sodiation, which forms a final sodiated phase of $Na_{1.6}Ge$,[18] agreeing with that of the Ge thin film electrode. They found that the initial sodiation process amorphizes the Ge nanowire while pores were formed in Ge nanowires after the desodiation. By comparing the Li-based and the Na-based systems, it is found that the dealloying of the sodiated Ge nanowires results in larger pores.[18] In the field of metallurgy, the formation of pores is a common phenomenon in selective dealloying processes.[76] The porosity will likely modify the mechanical properties of electrodes, thus affecting the cycling performance.[13b]

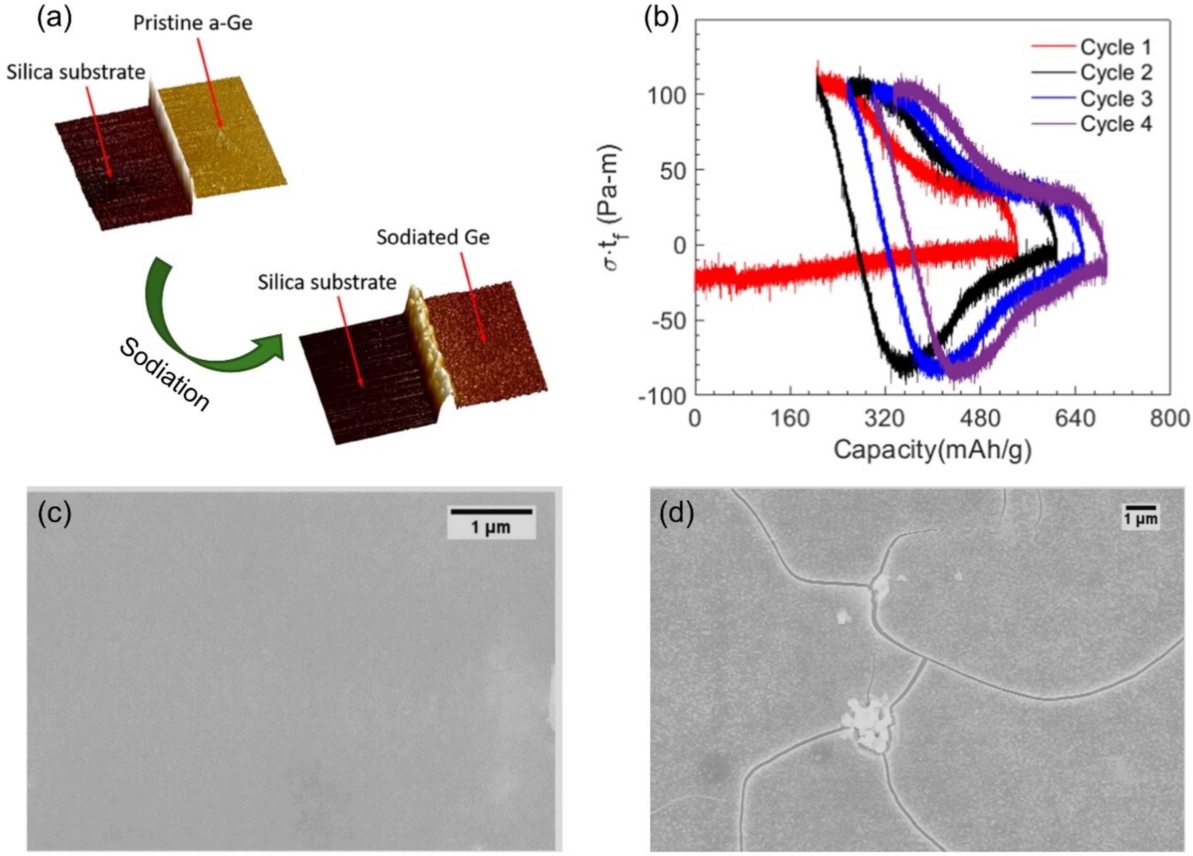

Figure 10. (a) AFM image of the pristine α-Ge film and the film at the end of 1st sodiation process. (b) Stress-thickness behavior of a-Ge thin film anode as a function of specific capacity, respectively, during sodiation/desodiation under galvanostatic cycling (at a constant current density of ~1 μAcm^{-2}, i.e., at C/20 rate). The Ge thin films have a thickness of 100 nm (1 Pa-m = 10^{-3} GPa in the given system). Surface morphology revealed by scanning electron microscopy (SEM): (c) As-deposited and (d) cycled (×5) Ge thin film electrodes. Adapted 2021 CC BY 4.0.[44]

Mechanical Properties of Na-Ge Phases. Papakyriakou et al., relying on the nanoindentation technique, found that the modulus and hardness of $Na_{0.6}Ge$ are notably smaller than those of the pristine **Ge thin film**.[77] The theoretical predictions are also consistent with these experimental results. Based on the first principle calculations, Chou et al. estimated that the bulk modulus of sodiated amorphous NaGe decreases by 40.4%, as compared to that of elemental Ge.[25a] In a different computational work, Mortazavi et al. reported a similar softening behavior, evidenced by the changes in elastic (*E*), bulk (*B*), and shear (*G*) moduli in the Na–Ge system as the Na content increased from 0 to 1 (Table 2),[25b] leading to a smaller *B/G* ratio of ~0.88 for NaGe (vs. 1.32 for Ge), which is indicative of a more brittle nature.

Electrode Stability during Electrochemical Cycling. The significant volume expansion and associated mechanical stress evolution during the sodiation of Ge appear to hinder satisfactory cycling performance. Abel et al. compared the cycling performance of the two **Ge thin film** electrodes prepared by electron beam deposition with two different substrate incident angles, referring to the dense Ge film and the nanocolumnar Ge film. Surprisingly, the former begins to exhibit noticeable capacity decay after only 15 cycles while the latter shows a significantly stable cycling behavior, giving 100 cycles with 88% capacity retention.[42] A recent study reported that the **Ge composite** electrode consisting of 70 wt% ball-milled amorphous Ge nano-powder (10 nm) experienced a significant capacity fade after 40 cycles.[78] Systematic investigations into cycling performance of Ge anodes are recommended for future research.

3.3.3. Na-Sn System

Volume Change, Structure Evolution, and Mechanical Stress. A DFT calculation by Chevrier et al. suggested that a more than 400% volume expansion could be induced after the sodiation to $Na_{15}Sn_4$.[57] Zhang et al. calculated the volume change caused by the molar volume of the incorporated Na to be approximately 130%, 250%, and 430%, for NaSn, Na_9Sn_4, and $Na_{15}Sn_4$, respectively.[53]

Experimentally, the **Sn thin film** electrode is reported to undergo a significant volume expansion during sodiation, resulting in a transition from a generally flat surface (Figure 11a) to a porous morphology with pore sizes ranging from 0.2 to 1.8 μm (Inset of Figure 11b). This pore formation during the incorporation of Na(Li) is not quite common because pores are often formed during selective dealloying processes at high rates.[76] It is speculated that the possible gas formation due to the electrolyte decomposition catalyzed by Sn should be responsible,[79] but the underlying mechanisms warrant further investigation. Moving to desodiation, obvious cracking is only observed until the electrode potential hits the second plateau at ~0.28 V vs. Na/Na^+ (Figure 11c-d).

By measuring the **Sn foil** electrode thickness at different sodiation states, Zhu et al. quantified the volume change for the $Sn/NaSn_3$, Sn/NaSn, Sn/Na_9Sn_4, and $Sn/Na_{15}Sn_4$ transition to ~100%, ~120%, ~250%, and ~430%, respectively,[80] generally consistent to the calculated values mentioned above. However, it should be noted that these quantifications were made only considering the thickness change, i.e., the expansion along the z-axis during the sodiation. An SEM work examined the surface morphological changes (Figure 11e-f) of 60 μm- and 500 μm-thick Sn foil electrodes during cycling, and found that whiskers (red arrows in the inset of Figure 11f) appear in the 500 μm-thick foil after 5 partial cycles in addition to 'dry lake' fractures.[81] Differently, while the 60 μm-thick foil also exhibits

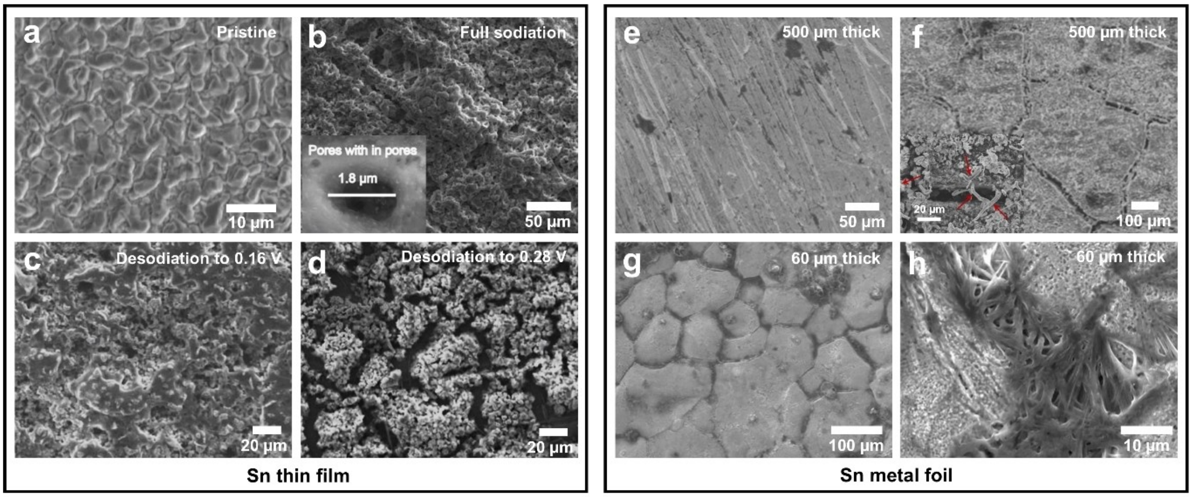

Figure 11. SEM images of the Sn thin film (~1 μm in thickness) electrode: (a) before cycling and (b) after a full sodiation at 0.005 V vs. Na/Na^+. The inset shows an enlarged view to reveal the pore formation. Then SEM images were taken again after a partial desodiation until (c) 0.16 and (d) 0.28 V vs. Na/Na^+. Adapted with permission 2019 American Chemical Society.[79] SEM images of 500 μm thick Sn metal foils are also provided to illustrate the surface morphology (e) before cycling and (f) after five cycles. The red arrows in the inset indicate the Sn whiskers formed after cycling. (g-h) SEM images of a thinner Sn foil (60 μm) after five cycles are shown to visualize cracks and pores. Adapted with permission 2019 American Chemical Society.[81]

similar fractures (Figure 11g), pores are formed instead of whiskers (Figure 11h),[81] suggesting that the thickness may be a factor in determining the morphological characteristics of the Sn foil electrodes.

The volume expansion of **Sn composite** electrodes may be more representative in the absence of misfit strain (thin films deposited on substrates) and mechanical stress at the phase boundary (thick metallic foils). Wang et al., based on the TEM observation, reported that the initial sodiation of Sn nanoparticles caused a volume expansion of 54–63 % upon the formation of the $NaSn_2$ phase, whereas larger volume changes of 210–280 % and 402 %-459 % were induced after the sodiation to the higher-order Na_9Sn_4 and $Na_{15}Sn_4$ phases.[52] An in-situ hard X-ray nanotomography visualized an approximately 326 % volume expansion by the end of sodiation of the Sn particle upon the formation of Na_9Sn_4 or higher-order Na_xSn ($x > 2.25$) phase. This study has also defined the critical size of Sn particles to be ca. 0.5 μm for fractures with low complexity and ca. 1.6 μm for fractures with high complexity,[58] indicating that the extent of mechanical damage in Na–Sn composite electrodes seems to be related to their particle size. Noteworthy, the dependency of electrode damage on the Sn particles size is also reported by Wang et al., but differently, he found that only Sn particles with a size larger than 100 nm underwent significant fracture, suggesting that the critical size for Sn particles to suppress fracturing should be below ca. 100 nm.[52] This claim seems to be verified by another study on Sn–C composite electrodes with Sn particles of ca. 90 nm (estimated by XRD using the Scherrer equation), where no obvious fracture was found in the electrode after 20 cycles.[82]

For **Sn pillars**, a similar volume expansion of ca. 400 % was documented, agreeing with the other electrode architectures. Meanwhile, an isotropic expansion behavior during sodiation was observed in crystalline Sn pillars.[83] Byeon et al. further compared the sodiation behavior of single crystalline Sn pillars with three crystallography orientations, i.e., <100>, <101>, and <211>. Based on SEM images, it is found that all the Sn pillars experienced the same isotropic swelling upon sodiation, regardless of their orientations (Figure 12).[26] In literature, this isotropic expansion behavior upon sodiation/lithiation is not observed in some other alloy anodes. For example, Sb pillars expand anisotropically upon sodiation to transform a circular cross-section into a non-circular and irregular shape, which is named by the authors as a 'dumbbell' shape.[83] In Li-based systems, lithiation of Si and Al was also found to be anisotropic with preferential volume expansion along certain crystallographic directions.[41,84]

Mechanical Properties of Na-Sn Phases. Mortazavi, et al., based on the DFT calculations, predicted a remarkable decrease in the elastic modulus of the Na_xSn alloy with an increasing Na content (Table 3), which is suggested to be caused by the transition from the Sn–Sn bonds (weakly covalent) to the Na–Sn bonds (weakly ionic).[25b] A similar monotonical reduction in the elastic modulus (E) of Na–Sn alloys was also suggested by Zhu et al. using the DFT calculation.[80] Concerning bulk modulus (B) and shear modulus (G), they were both estimated to show a nearly decreasing trend as the Na content increases.[25b,80] However, the B/G ratio for multiple Na–Sn intermetallic compounds, which can considered an indicator to distinguish whether a material is ductile (>1.75) or brittle (<1.75) based on Pugh's criteria, are all centered around 2 (Table 3).[87] Therefore, it seems difficult to suggest which of the Na–Sn intermetallic phases behave as ductile or brittle based on these theoretical calculations. It is worth noting that cracks were often observed in the Sn electrode after (de—)sodiaion,[81] probably indicating the brittle nature of Na–Sn phases, although no work has directly reported the true mechanical properties of Na–Sn intermetallic phases using experimental methods like mechanical indentation tests.

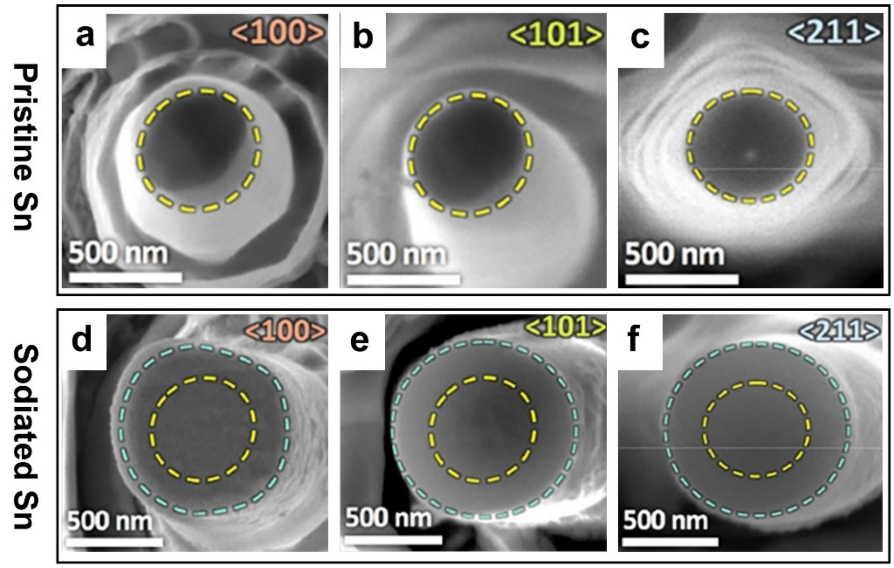

Figure 12. Cross-sectional morphologies of pristine and sodiated Sn nanopillars with different orientations: (a, d) <100>, (b, e) <101>, and (c, f) <211>. Adapted with permission 2018 American Chemical Society.[26]

Electrode Stability during Electrochemical Cycling. As evidenced by the degradation modes discussed above, such as the formation of cracks, whiskers, and pores, Sn electrodes in SIBs are speculated to be unstable during electrochemical cycling.

Nam et al. found that the electrodeposited **Sn thin film** electrode decays quickly and only retains ~20% of its initial capacity after 21 cycles.[88] Consistently, as shown in Figure 13a, the capacity of a 50 nm-thick Sn film electrode that was cycled between 0.001 V and 1 V vs. Na/Na^+, degrades from 830 mAh g^{-1} to 360 mAh g^{-1}, 144 mAh g^{-1}, and 61 mAh g^{-1}, after 10th, 20th, and 50th cycle, respectively.[28b] The associated SEM images of the pristine and cycled Sn film are given in Figure 13b-c, in which the morphological change is suggested to be responsible for the capacity degradation. Surprisingly, the authors found that the cycling stability of the same Sn thin film is significantly improved by limiting the desodiation potential below 0.8 V vs. Na/Na^+, giving a ~93% capacity retention as compared to ~13% with a desodiation potential cutoff at 1 V vs. Na/Na^+. While the mechanistic reasons behind this improvement warrant further investigation, the authors suggested that desodiation of the Sn electrodes beyond 0.8 V vs. Na/Na^+ might result in the formation of Sn^{Z+} surface species, which may be responsible for the poor cycling stability.[28b]

For the **Sn foil** electrodes, our group observed that the 30 μm-thick Sn foil stopped functioning after only 2–3 complete cycles, and the electrode suffered from severe mechanical damage after the initial cycle: Significant cracks and voids are formed during the (de−)sodiation process, and the structural integrity of the Sn foil can be hardly maintained. Inconsistently, Kim et al. reported that the cold-rolled Sn foil electrodes can maintain ~90% of initial capacity after 100 cycles at 0.1 C (Figure 13d). Based on SEM observations, the Sn foil electrode that underwent electrochemical cycling first pulverized into many nanoparticles and then reconnected to form a porous coral-like structure due to its self-healing nature (Figure 13e-f), contributing to the decent cyclability.[89]

With respect to **Sn composite** electrodes, they can survive longer up to one hundred cycles with the assistance of reliable binders and additives. Garayt et al. reported 200 stable cycles of the Sn particle electrode (Figure 13g) with 820 mAh g^{-1} reversible capacity. The excellent cycling stability was suggested to be associated with the restructuring of Sn particles from tens of microns (pristine) to roughly 1 μm (after tens of cycles) (Figure 13h-i). The authors suggested further investigation into

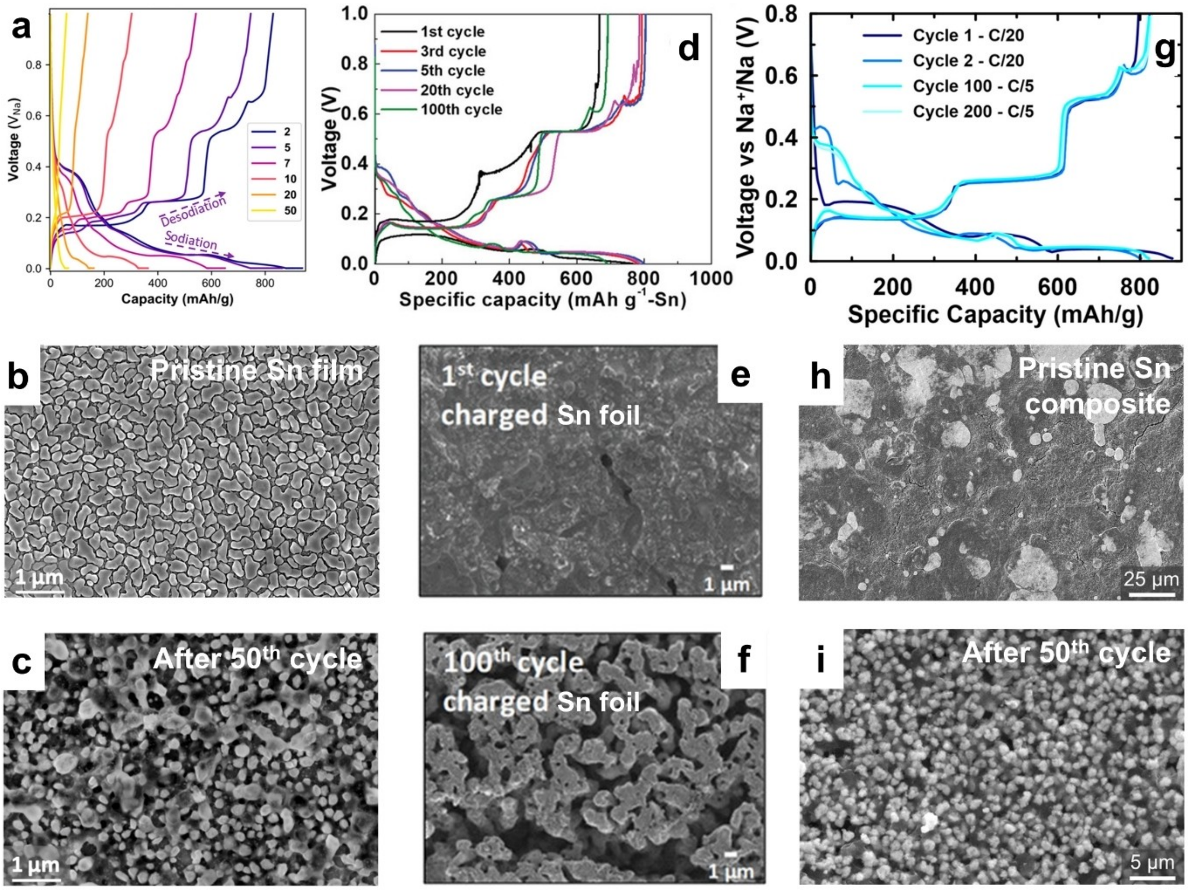

Figure 13. Galvanostatic cycling profiles in conjunction with SEM observations of Sn-based electrodes with different architectures: (a-c) Sputtered Sn film with a thickness of ~50 nm. Adapted with permission 2020 American Chemical Society.[28b] (d-f) Cold-rolled Sn foil with a thickness of ~25 μm. Adapted with permission 2021 John Wiley and Sons.[89] (h-i) Sn composite electrode consisting of 79.5% Sn powder (100 mesh) 9.4% carbon black, 9.9% PAANa binder, and 0.5% single wall carbon nanotube (SWCNT). Adapted 2024 CC BY 4.0.[92]

why Sn particles stabilize at a one-micron scale without experiencing pulverization.[61] Consistently, a microscopy study revealed that the micro-sized Sn powders transform into Sn nanoparticles via severe mechanical deformation with pores and voids during the early cycles. The authors also emphasized the critical role of SEI in the cycling performance of Sn composite electrodes in SIBs.[90] The selection of proper electrolytes may offer effective solutions to the prolonged cycling lives of Sn composite electrodes. Du et al. identified two ether-based electrolytes for the growth of stable SEIs, which led to 100 stable cycles of the Sn composite electrodes.[91]

3.3.4. Na-Pb System

Volume Change, Structure Evolution, and Mechanical Stress. Based on the molar volume of Na–Pb intermetallic phases, it is estimated that the sodiation to $Na_{15}Pb_4$ could yield a volume expansion of ~358%, with volume expansions of ~26%, ~100%, and ~216%, for the formation of intermediate $NaPb_3$, NaPb, and Na_9Pb_4, respectively.[63–64] Our group recently characterized the **Pb foil** electrode using ex-situ SEM and XRD techniques. As shown in Figure 14a and 14d, the metallic surface of the Pb foil is mostly covered with sodiated phases that exhibit a darker color at 5% sodiation depth. When the sodiation proceeds to 80%, the Pb foil largely maintains its integrity though its surface morphology changed completely to spherical protrusions with cracks on top (Figure 14b and 14e). Figures 14c and 14f indicate that 100% sodiation seems to

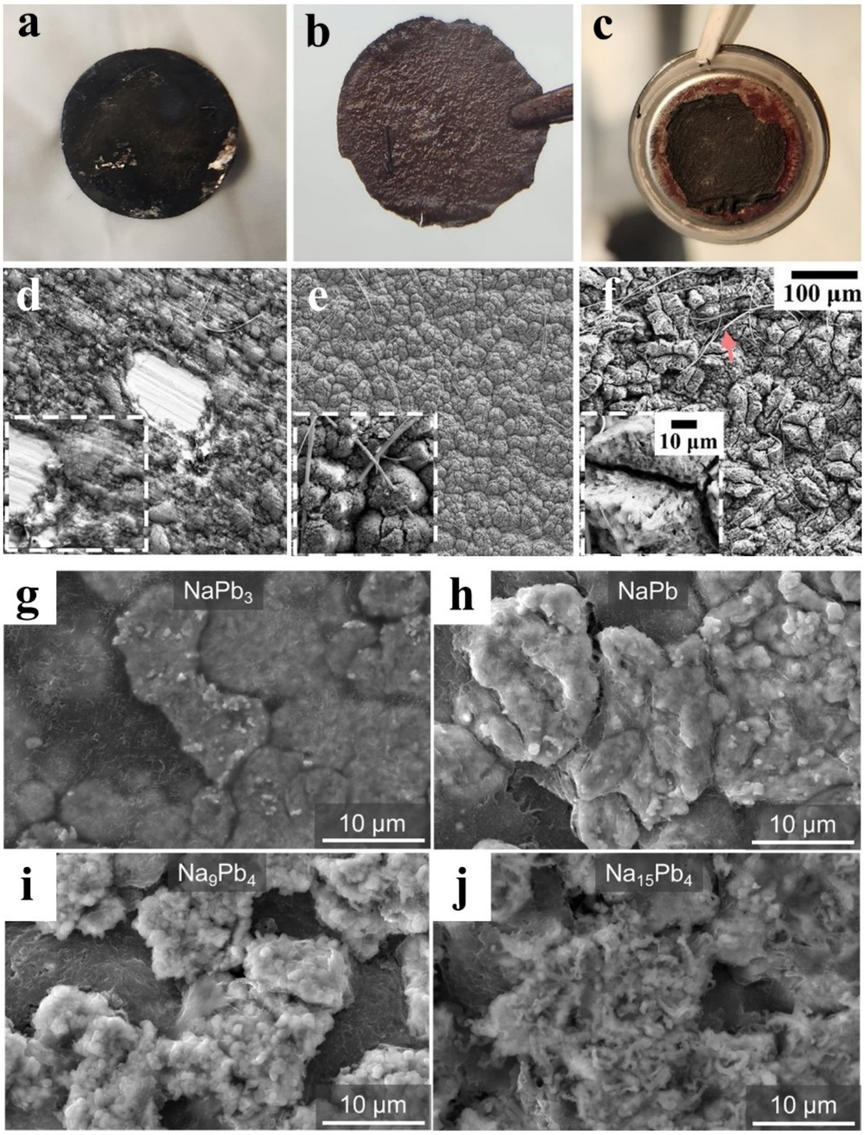

Figure 14. Photographic and SEM images of the 30 µm-thick Pb foil electrode at (a, d) 5%, (b, e) 80%, and (c, f) 100% sodiation depth, revealing the structural evolution. Adapted 2024 CC BY 4.0.[64] Top-down SEM images of the Pb composite electrode that is approximately at (g) the $NaPb_3$ phase, (h) the NaPb phase, (i) the Na_9Pb_4 phase, and (j) the $Na_{15}Pb_4$ phase. Reprinted 2024 CC BY 4.0.[63]

cause more catastrophic cracking. The study suggests that the desodiation process may be more problematic, transforming a dense foil into a porous and mossy structure.[64]

Garayt et al. studied the **Pb composite** electrode following each phase transformation during sodiation. Figure 14g shows that the formation of $NaPb_3$ does not alter the structure of Pb particles under an electron microscope. Further sodiation to the NaPb phase shown in Figure 14h leads to slight fissures within Pb particles. More drastic structure evolution is observed upon the formation of higher ordered Na_9Pb_4 and $Na_{15}Pb_4$ phases (Figure 14i-j), which involve a significant restructuring of Pb particles from 20 μm to sub-micron sizes.[63] To date, few experimental works are available regarding the mechanical stress induced by Na insertion/extraction into/from Pb electrodes.

Mechanical Properties of Na-Pb Phases. As predicted by Mortazavi et al.,[25b] based on the first-principle simulation, the elastic (*E*), bulk (*B*), and shear (*G*) moduli show a decreasing trend toward the increasing Na content (Table 3). However, the *B/G* ratios do not exhibit a monotonic correlation with the Na content in the Na–Pb phases. The *B/G* values of Pb and $NaPb_3$ are greater than 3, significantly higher than 1.75 (the transition point from brittleness to ductility based on Pugh's criteria),[68] suggesting their ductile nature, while the *B/G* value of Na_xPb ($x \geq 1$) is between 1.5-2. Recently, Garayt et al. synthesized the Na–Pb intermetallics (i.e., $NaPb_3$, NaPb, Na_9Pb_4, and $Na_{15}Pb_4$) by Na-milling of Pb powders followed by vacuum-sintering and examining the brittleness of these alloys by pressing them with the motor and pestle in the glovebox. They found that while Pb and $NaPb_3$ are ductile, the Na-rich Na–Pb intermetallic phases (i.e., NaPb, Na_9Pb_4, and $Na_{15}Pb_4$) are likely brittle (Table 3).[63]

Electrode Stability during Electrochemical Cycling. Zhang et al. recently conducted a systematic study on the reversibility of **Pb foil** electrodes in SIBs. Due to the observed cracking after sodiation and loss of electrode integrity after desodiation, the Pb foil electrodes often stop functioning after a handful of cycles upon full utilization. In consequence, the authors propose a partial sodiation approach for Pb foil electrodes, giving 140 stable cycles when the cycling is limited between Pb and $NaPb_3$.[64] Similarly, as shown in Figure 15a, the Pb foils with two different thicknesses exhibit unstable cycling behavior and

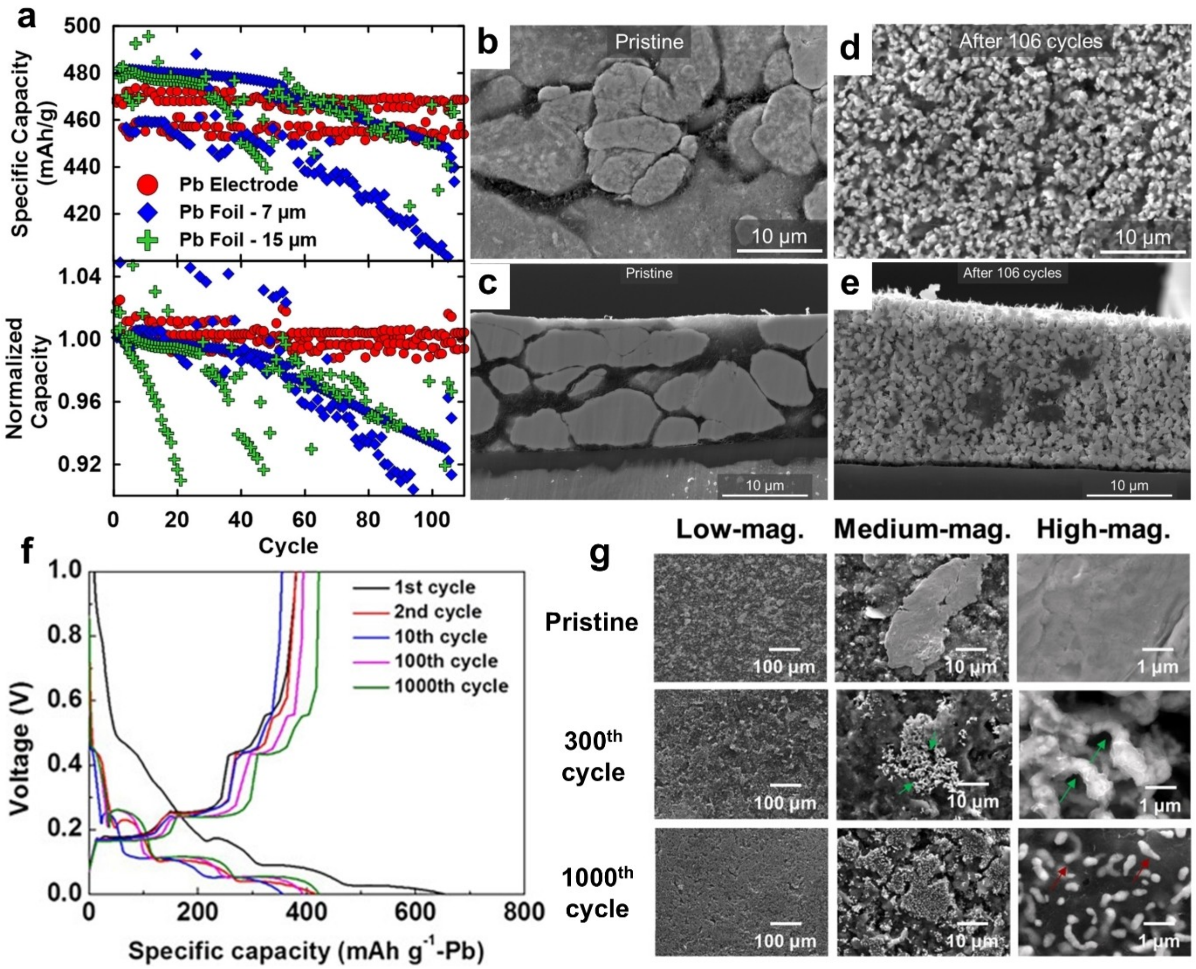

Figure 15. (a) Cycling performance of the Pb composite electrode (red) in comparison with two Pb foils. SEM images of the Pb composite electrode before and after cycling: (b, d) Top view and (c, e) cross-sectional view. Adapted 2024 CC BY 4.0.[63] (f) Galvanostatic charge-discharge curves at 10 C representing a decent cycling stability of the Pb composite electrode. (g) SEM images taken along with the long-term cycling test, including pristine, 300th, and 1000th cycles. Adapted with permission 2021 Elsevier B.V.[93]

often experience large inconsistencies in capacity between neighboring cycles.[63]

The cycling performance of the SWCNT-decorated **Pb composite** electrode in Figure 15a (red dots) is better, giving 106 stable cycles. Based on the SEM examination, the promising cycle life is suggested by Garayt et al. to originate from the microstructural change of the Pb particles. As illustrated in Figure 15b-e, pristine Pb particles with a size of tens of microns restructure and evolve to form nanosized particles after 106 cycles in the absence of obvious cracks or other failure modes. Consistently, Kim et al. reported a remarkable cycling performance of the multi-wall CNT (MWCNT) micro-sized Pb particles, which can be cycled 1000 times without significant capacity degradation (Figure 15f). A similar description is given, referring to a self-healing process: The Pb particles were initially disintegrated into many nanosized ones during the electrochemical cycling, and subsequently these nanoparticles reconnected together to form a coral-like structure and finally fiber-shaped Pb particles. As indicated by the arrows in Figure 15g, the restructured and nanosized Pb particles are easily embedded into the conductive matrix, i.e., MWCNT, which could function as a buffer to accommodate their volume expansion, thereby giving a stable cycling.[93] While the difference in the cycling performance of Pb foil and Pb particle electrodes is worth further investigation, it is suggested to be related to the variation of Na diffusion kinetics caused by the electrode architecture.[63–64]

3.4. Kinetics of Na-M_{IVA} System

In SIB cells, the electrochemical reaction primarily consists of various processes such as the de-solvation of Na^+ in liquid electrolytes, the Na transport through the SEI layer, the electron transport from the current collector through the electrode to the interface, and the Na diffusion in solid electrodes. Any factors limiting these processes will impede the reaction kinetics and affect the electrochemical performance. Understanding the nature of sodiation and the origin of kinetical limitation is the key to the design and development of electrode materials. Here we mainly summarize the possible limiting factors for the sodiation kinetics of Si, Ge, Sn, and Pb electrodes.

3.4.1. Na-Si System

For the Na–Si system, regardless of the electrode architecture, no electrochemical sodiation has been demonstrated experimentally to date. Many studies attributed this unsuccessful sodiation to sluggish kinetics but warrant further verification.[25a,34,94]

3.4.2. Na-Ge System

An investigation of **Ge thin film** electrodes indicated that the sodiation is limited kinetically rather than thermodynamically, as evidenced by preferred phase transformations at elevated temperatures or slower C-rates.[27] Furthermore, systematic potentiostatic measurements were conducted to provide insights into the nature and kinetics of each phase transformation involved in the sodiation of the Ge film electrodes. For the Ge/$NaGe_4$ phase transformation, the current-time curves are found to be featured by a "kink" (arrow in Figure 16a) that divides the sodiation process into two stages. These potential dependent "kinks" suggest that the early sodiation of Ge to $NaGe_4$ probably occurs via the propagation of a sharp interface from the film surface to the current collector. By contrast, in the case of the $NaGe_4$/$Na_{1+x}Ge$ transformation, the current-time curves exhibit a "current hump" characteristic (Figure 16b). Namely, after applying an electric potential, the current responses increase almost instantaneously until reaching the maximum values followed by monotonous decreases. This electrochemical feature is indicative of the nucleation-growth mechanism for the $NaGe_4$/$Na_{1+x}Ge$ transformation. Through the interpretation of Avrami parameters, the authors suggested that the transformation of Ge to $NaGe_4$, following a one-dimensional model, is largely governed by Na diffusion, whereas the transformation from $NaGe_4$ to $Na_{1+x}Ge$ is controlled by the reaction at the phase front. Based on the Cottrell equation, the Na diffusion coefficient in $NaGe_4$ is calculated to be in the order of $\sim10^{-12}\,cm^2\,s^{-1}$ at room temperature.[27] Additionally, by correlating the rate constants with the sodiation temperature, the activation energy for the reactions of Ge/$NaGe_4$, and of $NaGe_4$/$Na_{1+x}Ge$ was estimated to be roughly 50 and 70 $kJ\,mol^{-1}$ (Figure 16c-d), respectively.[27]

Lu et al., employing the in-situ TEM technique, investigated the sodiation nature and kinetics of the **Ge nanowire** electrode.[18] As illustrated in Figure 16e, the chemical sodiation of Ge nanowires occurs through the movement of a V-shaped Na diffusion front. Moreover, the square of the sodiation distance (L) of Ge nanowires was found to be approximately proportional to the sodiation time, suggesting that the sodiation behavior of Ge is characterized by a diffusion-controlled reaction (DCR) mechanism.[18] By roughly dividing the sodiation distance by time, the sodiation rate along the length and radial directions of the nanowires were determined to be roughly 1903 $nm\,min^{-1}$ and 740 $nm\,min^{-1}$, respectively. These values are significantly higher than the ones (860 $nm\,min^{-1}$ and 450 $nm\,min^{-1}$) obtained from chemical lithiation of the same nanowires.[18]

3.4.3. Na-Sn System

Byeon et al. observed a dramatic increase in the electrical resistance of a partly sodiated **Sn foil** electrode (roughly corresponding to the formation of the NaSn phase) by 6 orders of magnitudes (Figure 17a), suggesting that the formation of the electrochemically resistive NaSn intermediate phases im-

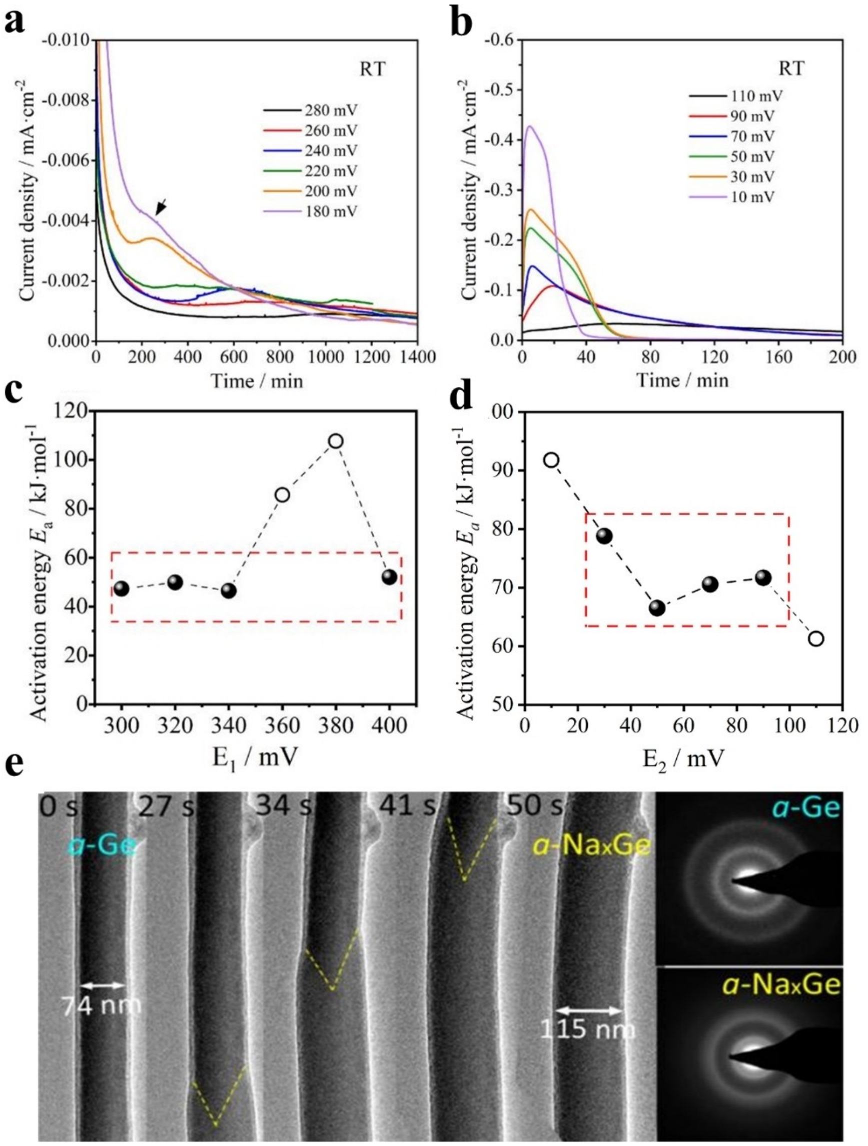

Figure 16. (a) The current-time curves of the Ge thin film electrode at the different applied potentials after the initial hold at 600 mV (vs. Na/Na$^+$) during the chronoamperometry measurements, and (b) the current-time curves of the Ge thin film electrode at the different applied potentials after the initial hold at 250 mV (vs. Na/Na$^+$). The calculated activation energy for (c) the Ge/NaGe$_4$ and (d) the NaGe$_4$/Na$_{1+x}$Ge phase boundary movement by Arrhenius equation at different potentiostatic holds. Adapted 2023 CC BY 4.0.[27] (e) The TEM images of the amorphous Ge nanowires recorded at different sodiation times. Adapted with permission 2016 American Chemical Society.[18]

pedes the charge transfer process and degrades the electrode capacity due to a high Coulombic loss.[73] Consistently, Choi et al. also found that the electrical resistance of Na–Sn electrodes increased dramatically by 8 orders of magnitudes after the deep sodiation to the amorphous Na$_{3.75}$Sn phase (Figure 17b).[95] Both studies reported that the electrical resistance can reach a level as high as ~10^8 Ω upon sodiation. An ab initio simulation analysis indicated that the mechanical stress developed in the alloying of Sn with Na, caused the Zintl ions to distort from ideal configurations, which leads to changes in electronic structure and thereby an increased resistance of the sodiated Sn.[95] A revisit of the electrical resistance of the Na–Sn system using a thermodynamic model confirmed that both the multiple phase transitions and the formation of highly resistive Na–Sn phases are responsible for the poor kinetics and large energy loss of Sn foil electrodes.[30]

Regarding **Sn composite** electrodes, the inclusion of binders and conductivity enhancers may alter electrode kinetics, as compared to metallic Sn foils. Sarkar et al. systematically investigated the impacts of different binders, i.e., carboxymethyl cellulose (CMC) or polyvinylidene fluoride (PVDF), on the charge transfer and Na diffusion kinetics in Sn electrodes using the galvanostatic intermittent titration technique (GITT). The Sn composite electrodes with the CMC binder were found to perform better than the ones with the PVDF binder, as evidenced by a lower charge transfer resistance and a higher Na diffusion coefficient. Additionally, the electrolyte salt was also found to affect the sodiation kinetics of Sn composite

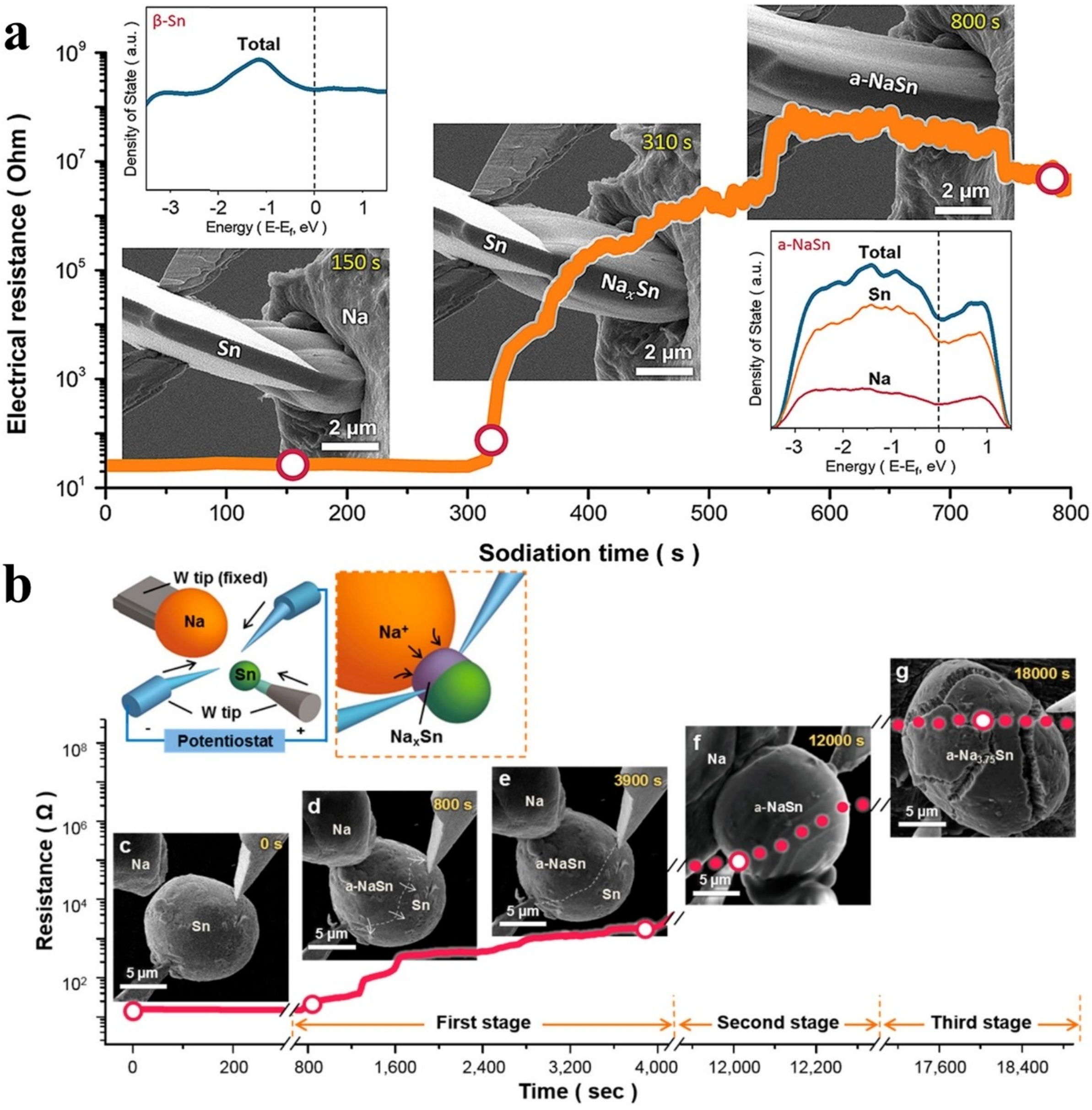

Figure 17. Changes in electrical resistivity and the morphology of the sodiated Sn as a function of the sodiation time: (a) Sn foil (Reprinted with permission 2017 Elsevier B.V.[73]) and (b) Sn particles (Reprinted with permission 2017 American Chemical Society[95]).

electrodes, which exhibit a lower charge transfer resistance with the $NaClO_4$-based electrolyte than the $NaPF_6$-based ones. Quantitatively, the diffusion coefficient of Na in Sn electrodes with a CMC binder in the $NaClO_4$ salt and PC solvent ranged between ~10^{-10}-10^{-17} $cm^2\,s^{-1}$ (vs. ~10^{-12}-10^{-16} $cm^2\,s^{-1}$ in $NaPF_6$-based electrolyte) during the sodiation process and ~10^{-9}-10^{-17} $cm^2\,s^{-1}$ during the desodiation.[96] Noteworthy, these diffusivity values derived from the GITT results are much lower than the ones calculated based on the in-situ TEM analyses, i.e., ~10^{-9} $cm^2\,s^{-1}$ and EIS measurements.[26,79,83,86] All these diffusivity values are summarized in Table 4 for easy reference.

Scientists also employed other electrode architectures like **Sn nanopillars** to conduct kinetic studies. The sodiation of Sn nanopillars is reported to be isotropic following a DCR mechanism. Choi et al. observed that the propagation length of the Na_xSn/Sn interface is generally proportional to the square root of time (Figure 18a), indicating that the sodiation process is governed by DCR. Along <211> direction, the sodiation rate of the crystalline Sn nanopillar (Ø = 550 nm) is measured to be ~1.25 μm s^{-1}, more than 2 orders of magnitude faster than the lithiation rate of crystalline Si. The authors, based on the atomic simulations, suggested that the smaller bonding energy, combined with the transition to the amorphous Na_xSn phase upon the sodiation broadens the Na diffusion passage and facilitates faster sodiation.[86] Consistently, Byeon et al. compared the sodiation of three single crystalline Sn nanopillars with different crystallographic orientations and found that the sodiation speed is similar in all directions, suggesting the

Table 4. Summary of kinetic-related information on the Na–Ge and Na–Sn systems.

System	Electrode materials	Sodiation kinetics	Na diffusivity at RT / $cm^2\ s^{-1}$	Technique	Ref.
Na-Ge	Ge thin film	Mainly DCR	~10^{-12} (in $NaGe_4$)	CA	[27]
	Ge thin film (nanocolumnar)	DCR	~10^{-13}	EIS	[18,42]
Na-Sn	Sn particle (micro-sized)	N/A	~10^{-9}-10^{-17}	GITT	[96]
	Sn thin film	N/A	~3.9×10^{-14}	EIS	[79]
	Sn nanopillar	DCR	~2.1×10^{-9}	In-situ TEM	[83]
			~6.7×10^{-9}	In-situ TEM	[83,86]
			~4.9×10^{-9}	In-situ TEM	[26]

RT: Room temperature. N/A: Not applicable.

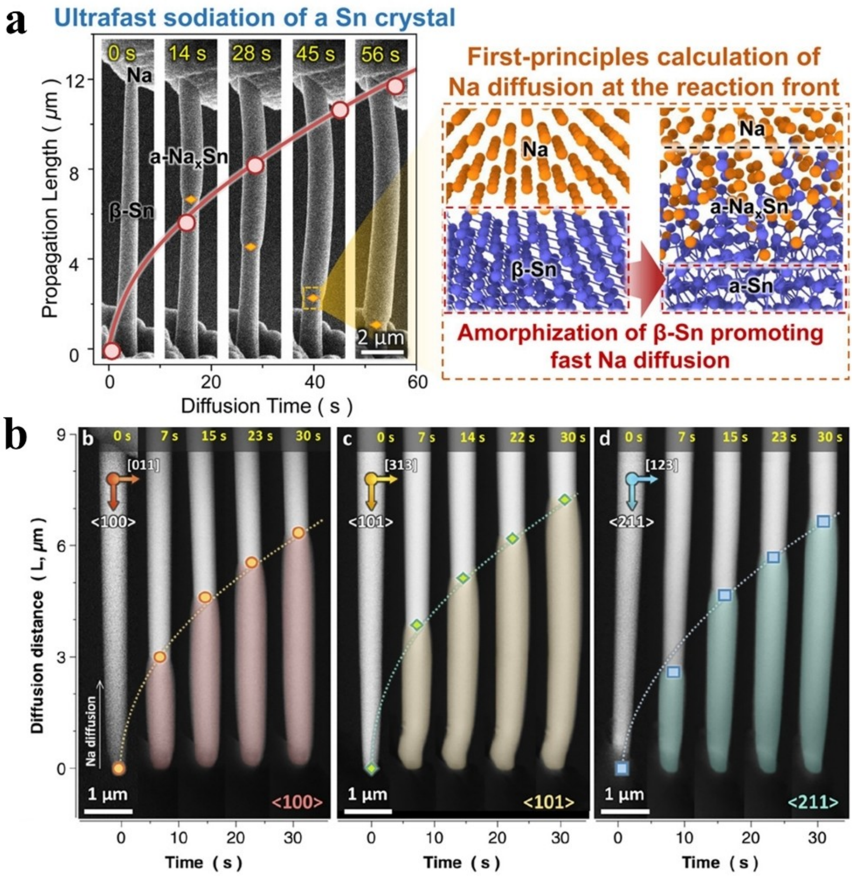

Figure 18. (a) TEM images of the Sn nanowires with the long axis along < 211 > during the sodiation and the simulation for the fast Na diffusion behavior. Reprinted with permission 2018 American Chemical Society.[86] (b) Comparison of sodiation of the Sn nanowires with different orientations. Reprinted with permission 2018 American Chemical Society.[26]

isotropic sodiation behavior of Sn. The proportional relationships (i.e., $L^2 \propto t$) are observed in all cases (Figure 18b), further strengthening that the sodiation of Sn nanopillars follows a DCR mechanism.[26]

Overall, the kinetic behaviors of Sn in regular electrode architectures remain unclear with a large range of diffusivity values reported, i.e., from 10^{-9} to 10^{-17} $cm^2 s^{-1}$. The Sn nanopillars, on the other hand, always exhibit diffusivities at the level of 10^{-9} $cm^2 s^{-1}$. It is noted that these values are extracted from the chemical sodiation, which may change during electrochemical sodiation with conventional electrode architectures, ionic electrolytes, and cell designs. Additionally, the diffusion kinetics may partly explain the isotropic volume expansion of Sn pillars during sodiation discussed above. Based on the DFT calculations, it is suggested that the sodiation creates a sharp interface between Sn and Na_xSn, which disrupts the < 100 > Sn crystal structure and leads to the amorphization of host Sn near the phase interface. This amorphization behavior weakens the orientation dependency of Na diffusion, leading to isotropic propagation of the phase front.[83]

3.4.4. Na-Pb System

It is demonstrated that the **Pb composite** electrode (98% Pb + 1% carbon additive + 1% PVDF) achieves a charging rate of as high as ~4 C (520 mA·g^{-1}) without sacrificing its capacity, indicating the fast sodiation kinetics of the micrometric Pb particles.[66] Consistently, the Pb composite electrode (70 wt% micro-sized Pb particles as active materials) prepared by Kim et al. also displays outstanding rate capability. Figure 19a shows that the Pb composite electrode is pushed to undergo galvanostatic (dis)charging at a C-rate as high as 25.6 C. Figure 19b makes it clear that the electrode can be cycled at 12.8 C without significantly sacrificing the reversible capacity. It is believed that the superior rate capability originates from the linear shape of the Pb particles, which results in a higher surface area in contact with the conductive matrix (i.e., MWCNTs) to a greater extent than that of spherical particles. In turn, the electrode kinetics should be facilitated by the enhanced electron pathways between the current collector and the Pb particles.[93]

Contradictorily, Park, et al. argue that the **Pb**@PbO-C **composite** electrode exhibits unfavorable sodiation kinetics. Based on the synchrotron-based X-ray diffraction and absorption analyses, it is suggested that the formed NaPb Zintl phase, which has a high electric resistance,[95] impedes the electron transfer of the Na alloying reactions and limits the Na transport. This claim is well supported by the smaller internal resistance estimated by dividing the overpotentials between the quasi-equilibrium and the closed-circuit potential from the GITT measurements.[100] While the experimental data regarding the electrical properties of Na-rich Na–Pb intermetallic phases at ambient temperature have not been published to date, some early studies have consistently shown that the electric resistance of the Na–Pb alloy increases as Na concentration goes up and reaches its maximum value at roughly Na_3Pb at high temperature (Figure 19c).[97–99] Therefore, it is reasonable to predict that the formation of more electrically resistive Na–Pb intermediate phases could negatively affect the charge transfer kinetics, thereby slowing down the sodiation process of Pb to some extent.

4. Summary and Recommendations

Group IVA elements offer the prospect of increasing the energy density of SIBs due to their attractive Na storage capability as anode materials. This report systematically reviews the electrochemistry during the phase transformations, the mechanical effects caused by volume changes, and the reaction kinetics during (de−)sodiation processes, aiming to offer a comprehensive overview of Na storage mechanisms of group IVA alloy anode candidates (Si, Ge, Sn, Pb). Here we summarize the key points of each element:

- Si seems electrochemically inactive to Na, although theoretical calculations propose the presence of Na–Si intermetallic compounds. The reason behind this inconsistency remains unclear. Research attributes the sluggish kinetics to be responsible but no successful sodiation is observed experimentally at elevated temperatures up to 80 °C.
- Ge can be sodiated electrochemically but only in its amorphous states or with low crystallinity. The NaGe phase with a 1-to-1 atomic ratio does not seem to be the final sodiation product. Instead, higher-ordered phases such as Na_3Ge can form under kinetically favorable conditions (at higher temperatures or lower C-rates). Sodiation of Ge can lead to compressive stress of hundreds of MPa, which drives mechanical failures like cracking, accounting for its limitations in cycling performance.
- Sn is generally well-studied as compared to other alloy anode candidates. While the formation of $Na_{15}Sn_4$ is considered the final sodiated phase, controversies remain regarding what intermediate Na–Sn phases in the crystalline or amorphous state are formed during the electrochemical cycling. The sodiation of Sn is isotropic and follows a DCR mechanism. In addition to the common degradation modes like cracks, voids, and pulverization that deteriorate the cycling stability, it is worth noting that the electrical resistance of Sn increases drastically as Na is incorporated, leading to a series of kinetic issues.
- Pb appears to be overlooked by academia due to its toxicity and environmental concerns, such that limited literature is available regarding its Na storage mechanisms and inconsistencies remain between the phase diagram and the electrochemical data. However, very promising cycling per-

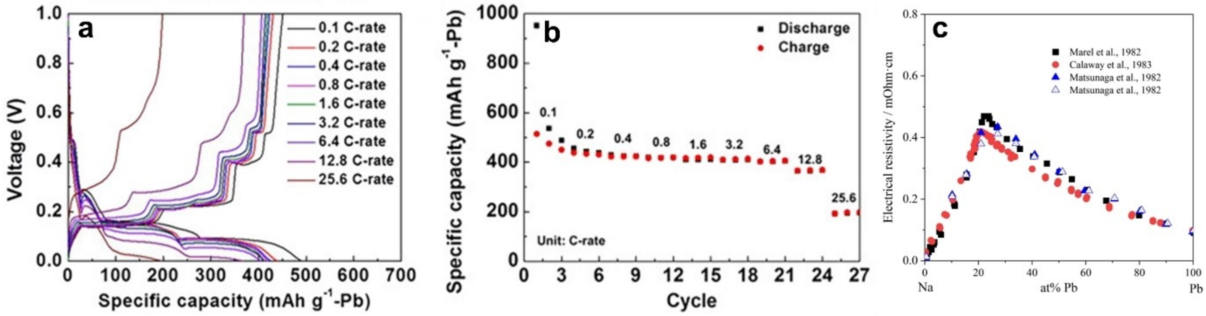

Figure 19. (a) Galvanostatic profiles of the Pb composite electrode at various C-rates, from which the specific capacity is plotted against cycle number in (b). Adapted with permission 2021 Elsevier B.V.[93] (c) The concentration-dependent resistivity of Na–Pb alloys at 10 °C (black solid square[97] blue solid triangle dots[98]) and 70°C (blue hollow triangle[98]) over the liquid line, and 723 K (red dots[99]).

formance is achieved with the Pb composite electrode owing to its self-restructuring nature.

Overall, except for Sn, a comprehensive understanding of other elements is still lacking. Hence future studies are recommended for each element:

- Si: The key reasons behind unsuccessful sodiation attempts should be uncovered by studying the interplay among synthesis, microstructure, and electrochemical performance of Si-based anode. High-energy ball-milling methods are worth exploring and may be used to unlock the sodiation of pure Si or Si oxides.[36,60a]
- Ge: The Na–Ge phases formed during sodiation appear to be amorphous, and thus require further verification using techniques other than regular XRD. Also, the cycling performance of Ge in SIBs is worth investigating.
- Sn: Given the literature on Sn in SIBs is rich, more engineering efforts are anticipated to improve the cycling performance for enabling practical applications. Future attempts to minimize the capacity loss of Sn anodes should focus not only on improving the electron and ion transport but also on mitigating the inhomogeneous distribution of Na concentration gradient and mechanical stress. Surface modification (e.g., carbon coating), compositing with carbonaceous materials (e.g., carbon nanotubes), and rational microstructure design (e.g., porous structure) could potentially be effective. Additionally, electrolyte optimizations (e.g., salt concentration, solvent composition, and additives) could be another strategy to prolong the lifetime of Sn anode by improving the ion diffusion kinetics and forming stable SEI layers.
- Pb: Together with the well-established recycling process, Pb should not have been neglected in the future roadmap of SIBs. More experimental research should be carried out to fill the research gap. By leveraging its availability, cost advantages, and recyclability, Pb may offer a practical solution to some of the challenges faced by SIBs.

List of Abbreviations

AFM	Atomic Force Microscopy
CA	Chronoamperometry
CMC	Carboxymethyl Cellulose
DCR	Diffusion-Controlled Reaction
DFT	Density Functional Theory
EIS	Electrochemical Impedance Spectroscopy
EVs	Electric Vehicles
FCC	Face-Centered Cubic
GCD	Galvanostatic Charge-Discharge
GITT	Galvanostatic Intermittent Titration Technique
HC	Hard Carbon
ICE	Initial Coulombic Efficiency
ICR	Interface-Controlled Reaction
LIBs	Lithium-Ion Batteries
MWCNT	Multi-Wall Carbon Nanotubes
NMR	Nuclear Magnetic Resonance
PABs	Pb-Acid Batteries
PBAs	Prussian Blue Analogues
PVDF	Polyvinylidene Fluoride
SEI	Solid-Electrolyte Interphase
SIBs	Sodium-Ion Batteries
TEM	Transmission Electron Microscopy
SEM	Scanning Electron Microscopy
SWCNT	Single-Wall Carbon Nanotubes
XRD	X-Ray Diffraction

Acknowledgements

J. Zhang would like to acknowledge the support from the Teaching Postgraduate Studentship (TPS) Scheme from the Department of Electrical and Electronic Engineering at The Hong Kong Polytechnic University (PolyU). T. Zheng acknowledges the support from the "PolyU Distinguished Postdoctoral Fellowship Scheme" (1-YWBT) and Photonics Research Institute (1-CDJ6) at PolyU. Both authors are grateful to W. Jin at PolyU for the financial support and to S. T. Boles from the Norwegian University of Science and Technology for the technical discussion.

Conflict of Interests

The authors declare no conflict of interest.

Keywords: Sodium-ion batteries · Alloy anodes · Phase transformations · Mechanical stresses · Electrode kinetics

[1] Z. J. Baum, R. E. Bird, X. Yu, J. Ma, *ACS Energy Lett.* **2022**, *7*, 712–719.
[2] M. Ma, S. Chong, K. Yao, H. K. Liu, S. X. Dou, W. Huang, *Matter* **2023**, *6*, 3220–3273.
[3] a) H. Kim, J. C. Kim, *eScience* **2024**, *4*, 100232; b) K. M. Abraham, *Solid State Ion.* **1982**, *7*, 199–212; c) Y. Yung-Fang Yu, J. T. Kummer, *J. Inorg. Nucl. Chem.* **1967**, *29*, 2453–2475.
[4] A. Yoshino, *Angew. Chem. Int. Ed. Engl.* **2012**, *51*, 5798–5800.
[5] P. K. Nayak, L. Yang, W. Brehm, P. Adelhelm, *Angew. Chem. Int. Ed. Engl.* **2018**, *57*, 102–120.
[6] Y. Kim, K.-H. Ha, S. M. Oh, K. T. Lee, *Chem. Eur. J.* **2014**, *20*, 11980–11992.
[7] P. Desai, J. Huang, D. Foix, J.-M. Tarascon, S. Mariyappan, *J. Power Sources* **2022**, *551*, 232177.
[8] a) F. Xie, Z. Xu, Z. Guo, M.-M. Titirici, *Prog. Energy* **2020**, *2*, 042002; b) X. Guo, D. van de Kleut, J. Zhang, C. Chen, X. Wang, T. Zheng, S. Boles, *JOM* **2024**, *76*, 3557–3566.
[9] N. Tapia-Ruiz, A. R. Armstrong, H. Alptekin, M. A. Amores, H. Au, J. Barker, R. Boston, W. R. Brant, J. M. Brittain, Y. Chen, M. Chhowalla, Y.-S. Choi, S. I. R. Costa, M. Crespo Ribadeneyra, S. A. Cussen, E. J. Cussen, W. I. F. David, A. V. Desai, S. A. M. Dickson, E. I. Eweka, J. D. Forero-Saboya, C. P. Grey, J. M. Griffin, P. Gross, X. Hua, J. T. S. Irvine, P. Johansson, M. O. Jones, M. Karlsmo, E. Kendrick, E. Kim, O. V. Kolosov, Z. Li, S. F. L. Mertens, R. Mogensen, L. Monconduit, R. E. Morris, A. J. Naylor, S. Nikman, C. A. O'Keefe, D. M. C. Ould, R. G. Palgrave, P. Poizot, A. Ponrouch, S. Renault, E. M. Reynolds, A. Rudola, R. Sayers, D. O. Scanlon, S. Sen, V. R. Seymour, B. Silván, M. T. Sougrati, L. Stievano, G. S. Stone, C. I. Thomas, M.-M. Titirici, J. Tong, T. J. Wood, D. S. Wright, R. Younesi, *J. Phys. Energy* **2021**, *3*, 031503.
[10] M. Zhang, Y. Li, F. Wu, Y. Bai, C. Wu, *Nano Energy* **2021**, *82*, 105738.
[11] C. Delmas, *Adv. Energy Mater.* **2018**, *8*, 1703137.
[12] V. A. Sethuraman, V. Srinivasan, A. F. Bower, P. R. Guduru, *J. Electrochem. Soc.* **2010**, *157*, A1253–A1261.

[13] a) H. Li, T. Yamaguchi, S. Matsumoto, H. Hoshikawa, T. Kumagai, N. L. Okamoto, T. Ichitsubo, *Nat. Commun.* **2020**, *11*, 1584; b) T. Zheng, D. Kramer, M. H. Tahmasebi, R. Mönig, S. T. Boles, *ChemSusChem* **2020**, *13*, 5910–5920.

[14] M. N. Obrovac, V. L. Chevrier, *Chem. Rev.* **2014**, *114*, 11444–11502.

[15] R. Mogensen, D. Brandell, R. Younesi, *ACS Energy Lett.* **2016**, *1*, 1173–1178.

[16] a) C. Kim, H. Kim, M. K. Sadan, M. Jeon, G. Cho, J. Ahn, K. Kim, K. Cho, H. Ahn, *Small* **2021**, *17*, e2102618; b) C. Kim, I. Kim, H. Kim, M. K. Sadan, H. Yeo, G. Cho, J. Ahn, J. Ahn, H. Ahn, *J. Mater. Chem. A* **2018**, *6*, 22809–22818; c) M. Song, C. Wang, D. Du, F. Li, J. Chen, *Sci. China Chem.* **2019**, *62*, 616–621.

[17] J. Ni, L. Li, J. Lu, *ACS Energy Lett.* **2018**, *3*, 1137–1144.

[18] X. Lu, E. R. Adkins, Y. He, L. Zhong, L. Luo, S. X. Mao, C.-M. Wang, B. A. Korgel, *Chem. Mater.* **2016**, *28*, 1236–1242.

[19] a) J. Sun, M. Li, J. A. S. Oh, K. Zeng, L. Lu, *Mater. Technol.* **2018**, *33*, 563–573; b) M. A. Ud Din, C. Li, L. Zhang, C. Han, B. Li, *Mater. Today Phys.* **2021**, *21*, 100486.

[20] T. Zheng, S. T. Boles, *Prog. Energy* **2023**, *5*, 032001.

[21] V. L. Chevrier, G. Ceder, *J. Electrochem. Soc.* **2011**, *158*, A1011.

[22] P. P. Lopes, V. R. Stamenkovic, *Science* **2020**, *369*, 923–924.

[23] K. Yanamandra, D. Pinisetty, A. Daoud, N. Gupta, *J. Indian Inst. Sci.* **2022**, *102*, 281–295.

[24] F. J. Himpsel, D. E. Eastman, P. Heimann, B. Reihl, C. W. White, D. M. Zehner, *Phys. B* **1981**, *24*, 1120–1123.

[25] a) C.-Y. Chou, M. Lee, G. S. Hwang, *J. Phys. Chem. C* **2015**, *119*, 14843–14850; b) M. Mortazavi, J. Deng, V. B. Shenoy, N. V. Medhekar, *J. Power Sources* **2013**, *225*, 207–214; c) J. Park, J. Han, J. Gim, J. Garcia, H. Iddir, S. Ahmed, G.-L. Xu, K. Amine, C. Johnson, Y. Jung, Y. Kim, S.-M. Bak, E. Lee, *Chem. Mater.* **2023**, *35*, 4171–4180.

[26] Y.-W. Byeon, Y.-S. Choi, J.-P. Ahn, J.-C. Lee, *ACS Appl. Mater. Interfaces* **2018**, *10*, 41389–41397.

[27] J. Zhang, T. Zheng, K.-w. E. Cheng, K.-h. Lam, S. T. Boles, *J. Electrochem. Soc.* **2023**, *170*, 100518.

[28] a) J. Songster, A. D. Pelton, *J. Phase Equilib.* **1992**, *13*, 67–69; b) S. Y. Sayed, W. P. Kalisvaart, E. J. Luber, B. C. Olsen, J. M. Buriak, *ACS Appl. Energ. Mater.* **2020**, *3*, 9950–9962.

[29] J. Sangster, A. D. Pelton, *J. Phase Equilib.* **1997**, *18*, 295–297.

[30] Y.-S. Choi, Y.-W. Byeon, J.-P. Ahn, J.-C. Lee, *J. Mater. Chem. A* **2018**, *6*, 9428–9436.

[31] a) J. Miao, C. V. Thompson, *J. Electrochem. Soc.* **2018**, *165*, A650–A656; b) J. Miao, B. Wang, C. V. Thompson, *J. Electrochem. Soc.* **2020**, *167*, 090557.

[32] W. Hume-Rothery, *J. Chem. Soc.* **1928**, 947–963, 10.1039/JR9280000947.

[33] L. Ellis, B. Wilkes, T. Hatchard, M. Obrovac, *J. Electrochem. Soc.* **2014**, *161*, A416.

[34] L. D. Ellis, B. N. Wilkes, T. D. Hatchard, M. N. Obrovac, *J. Electrochem. Soc.* **2014**, *161*, A416.

[35] S. Komaba, Y. Matsuura, T. Ishikawa, N. Yabuuchi, W. Murata, S. Kuze, *Electrochem. Commun.* **2012**, *21*, 65–68.

[36] M. Shimizu, H. Usui, K. Fujiwara, K. Yamane, H. Sakaguchi, *J. Alloys Compd.* **2015**, *640*, 440–443.

[37] S. C. Jung, D. S. Jung, J. W. Choi, Y.-K. Han, *J. Phys. Chem. Lett.* **2014**, *5*, 1283–1288.

[38] S. C. Jung, H.-J. Kim, Y.-J. Kang, Y.-K. Han, *J. Alloys Compd.* **2016**, *688*, 158–163.

[39] H.-Q. Wang, Y.-X. Zhao, L. Gou, L.-Y. Wang, M. Wang, Y. Li, S.-L. Hu, *Rare Met.* **2022**, *41*, 1626–1636.

[40] L. C. Loaiza, L. Monconduit, V. Seznec, *Small* **2020**, *16*, 1905260.

[41] T. Zheng, X. Wang, E. Jain, D. Kramer, R. Mönig, M. Seita, S. T. Boles, *Scr. Mater.* **2020**, *188*, 164–168.

[42] P. R. Abel, Y.-M. Lin, T. de Souza, C.-Y. Chou, A. Gupta, J. B. Goodenough, G. S. Hwang, A. Heller, C. B. Mullins, *J. Phys. Chem. C* **2013**, *117*, 18885–18890.

[43] L. Baggetto, J. K. Keum, J. F. Browning, G. M. Veith, *Electrochem. Commun.* **2013**, *34*, 41–44.

[44] S. Rakshit, A. S. Pakhare, O. Ruiz, M. R. Khoshi, E. Detsi, H. He, V. A. Sethuraman, S. P. V. Nadimpalli, *J. Electrochem. Soc.* **2021**, *168*, 010504.

[45] a) H. Ghassemi, M. Au, N. Chen, P. A. Heiden, R. S. Yassar, *ACS Nano* **2011**, *5*, 7805–7811; b) K. Kang, H.-S. Lee, D.-W. Han, G.-S. Kim, D. Lee, G. Lee, Y.-M. Kang, M.-H. Jo, *Appl. Phys. Lett.* **2010**, *96*, 053110.

[46] a) T. Zheng, J. Zhang, W. Jin, S. T. Boles, *ACS Appl. Energ. Mater.* **2023**, *6*, 1845–1852; b) T. Zheng, J. Zhang, X. Guo, W. Jin, S. T. Boles, *Electrochim. Acta* **2024**, *485*, 144127.

[47] L. Baggetto, P. Ganesh, R. P. Meisner, R. R. Unocic, J.-C. Jumas, C. A. Bridges, G. M. Veith, *J. Power Sources* **2013**, *234*, 48–59.

[48] L. D. Ellis, T. D. Hatchard, M. N. Obrovac, *J. Electrochem. Soc.* **2012**, *159*, A1801.

[49] T. Yamamoto, T. Nohira, R. Hagiwara, A. Fukunaga, S. Sakai, K. Nitta, S. Inazawa, *J. Power Sources* **2013**, *237*, 98–103.

[50] L. Baggetto, C. A. Bridges, J.-C. Jumas, D. R. Mullins, K. J. Carroll, R. A. Meisner, E. J. Crumlin, X. Liu, W. Yang, G. M. Veith, *J. Mater. Chem. A* **2014**, *2*, 18959–18973.

[51] Z. Du, R. Dunlap, M. Obrovac, *J. Alloys Compd.* **2014**, *617*, 271–276.

[52] J. W. Wang, X. H. Liu, S. X. Mao, J. Y. Huang, *Nano Lett.* **2012**, *12*, 5897–5902.

[53] B. Zhang, G. Rousse, D. Foix, R. Dugas, D. A. Dalla Corte, J. m. Tarascon, *Adv. Mater.* **2016**, *28*, 9824–9830.

[54] T. Yamamoto, T. Nohira, R. Hagiwara, A. Fukunaga, S. Sakai, K. Nitta, S. Inazawa, *J. Power Sources* **2012**, *217*, 479–484.

[55] Y. Grin, M. Baitinger, R. Kniep, H. v. Schnering, *Z. Kristallogr. New Cryst. Struct.* **1999**, *214*, 453–454.

[56] C. Kim, H. Kim, M. K. Sadan, M. Jeon, G. Cho, J. Ahn, K. Kim, K. Cho, H. Ahn, *Small* **2021**, *17*, 2102618.

[57] V. L. Chevrier, G. Ceder, *J. Electrochem. Soc.* **2011**, *158*.

[58] J. Wang, C. Eng, Y.-c. K. Chen-Wiegart, J. Wang, *Nat. Commun.* **2015**, *6*, 7496.

[59] J. M. Stratford, M. Mayo, P. K. Allan, O. Pecher, O. J. Borkiewicz, K. M. Wiaderek, K. W. Chapman, C. J. Pickard, A. J. Morris, C. P. Grey, *J. Am. Chem. Soc.* **2017**, *139*, 7273–7286.

[60] a) X. Zhang, L. Wang, T. Zheng, K.-h. Lam, *Batteries & Supercaps* **2023**, *6*, e202200495; b) X. Zhang, L. Wang, T. Zheng, K.-H. Lam, *Energy Fuels* **2023**, *37*, 11419–11431.

[61] M. D. Garayt, L. Zhang, Y. Zhang, M. C. Obialor, J. Deshmukh, Y. Xing, C. Yang, M. Metzger, J. Dahn, *J. Electrochem. Soc.* **2024**, *171*, 070523.

[62] a) T. Zheng, D. Kramer, R. Mönig, S. T. Boles, *ACS Sustain. Chem. Eng.* **2022**, *10*, 3203–3210; b) T. Zheng, D. Kramer, M. H. Tahmasebi, R. Mönig, S. T. Boles, *ChemSusChem* **2020**, *13*, 974–985.

[63] M. D. L. Garayt, M. C. Obialor, I. L. Monchesky, A. E. George, S. Yu, B. A. Rutherford, M. Metzger, J. R. Dahn, *J. Electrochem. Soc.* **2024**, *171*, 120521.

[64] J. Zhang, T. Zheng, X. Guo, H. Q. Nguyen, K.-w. E. Cheng, K.-H. Lam, D. Rettenwander, W. Jin, S. T. Boles, *J. Electrochem. Soc.* **2024**, *171*, 090516.

[65] T. R. Jow, L. W. Shacklette, M. Maxfield, D. Vernick, *J. Electrochem. Soc.* **1987**, *134*, 1730.

[66] A. Darwiche, R. Dugas, B. Fraisse, L. Monconduit, *J. Power Sources* **2016**, *304*, 1–8.

[67] a) A. Mukhopadhyay, B. W. Sheldon, *Prog. Mater. Sci.* **2014**, *63*, 58–116; b) M. K. Jangid, A. Mukhopadhyay, *J. Mater. Chem. A* **2019**, *7*, 23679–23726.

[68] P. Gandharapu, A. Mukhopadhyay, *Appl. Mech. Rev.* **2022**, *74*, 060802.

[69] T. Zheng, M. Muneeswara, H. Bao, J. Huang, L. Zhang, D. S. Hall, S. T. Boles, W. Jin, *ChemElectroChem* **2024**, *11*, e202400065.

[70] X. Gao, Y. Jia, W. Zhang, C. Yuan, J. Xu, *Appl. Mech. Rev.* **2022**, *74*, 060801.

[71] B. W. Sheldon, S. K. Soni, X. Xiao, Y. Qi, *Electrochem. Solid-State Lett.* **2011**, *15*, A9.

[72] Y. Zhu, C. Wang, *J. Phys. Chem. C* **2010**, *114*, 2830–2841.

[73] Y.-W. Byeon, Y.-S. Choi, J.-P. Ahn, J.-C. Lee, *J. Power Sources* **2017**, *343*, 513–519.

[74] a) A. Al-Obeidi, D. Kramer, C. V. Thompson, R. Mönig, *J. Power Sources* **2015**, *297*, 472–480; b) A. Al-Obeidi, D. Kramer, S. T. Boles, R. Mönig, C. V. Thompson, *Appl. Phys. Lett.* **2016**, *109*, 071902.

[75] S. P. V. Nadimpalli, R. Tripuraneni, V. A. Sethuraman, *J. Electrochem. Soc.* **2015**, *162*, A2840.

[76] Q. Chen, K. Sieradzki, *Nat. Mater.* **2013**, *12*, 1102.

[77] M. Papakyriakou, M. Lu, S. Xia, *J. Appl. Mech.* **2022**, *89*, 071007.

[78] C. Liu, Y. Jiang, C. Meng, X. Liu, B. Li, S. Xia, *Adv. Mater. Technol.* **2023**, *8*, 2201817.

[79] T. Li, U. Gulzar, X. Bai, M. Lenocini, M. Prato, K. E. Aifantis, C. Capiglia, R. Proietti Zaccaria, *ACS Appl. Energ. Mater.* **2019**, *2*, 860–866.

[80] Y. Zhu, Z. Qian, J. Song, W. Du, J. Pan, D. Wang, J. Yang, *Nano Lett.* **2021**, *21*, 3588–3595.

[81] T. Li, U. Gulzar, R. Proietti Zaccaria, C. Capiglia, S. A. Hackney, K. Aifantis, *J. Phys. Chem. C* **2019**, *123*, 15244–15250.

[82] M. K. Datta, R. Epur, P. Saha, K. Kadakia, S. K. Park, P. N. Kumta, *J. Power Sources* **2013**, *225*, 316–322.

[83] J.-H. Park, Y.-S. Choi, Y.-W. Byeon, J.-P. Ahn, J.-C. Lee, *Nano Energy* **2019**, *65*, 104041.
[84] S. W. Lee, M. T. McDowell, J. W. Choi, Y. Cui, *Nano Lett.* **2011**, *11*, 3034–3039.
[85] S. C. Jung, D. S. Jung, J. W. Choi, Y. K. Han, *J. Phys. Chem. Lett.* **2014**, *5*, 1283–1288.
[86] Y.-S. Choi, Y.-W. Byeon, J.-H. Park, J.-H. Seo, J.-P. Ahn, J.-C. Lee, *ACS Appl. Mater. Interfaces* **2018**, *10*, 560–568.
[87] S. Pugh, *Lond. Edinb. Dublin Philos. Mag. J. Sci.* **1954**, *45*, 823–843, 10.1080/14786440808520496.
[88] D.-H. Nam, K.-S. Hong, S.-J. Lim, T.-H. Kim, H.-S. Kwon, *J. Phys. Chem. C* **2014**, *118*, 20086–20093.
[89] C. Kim, H. Kim, M. K. Sadan, M. Jeon, G. Cho, J. Ahn, K. Kim, K. Cho, H. Ahn, *Small* **2021**, *17*, 2102618.
[90] A. Daali, X. Zhou, C. Zhao, I. Hwang, Z. Yang, Y. Liu, R. Amine, C.-J. Sun, W. Otieno, G.-L. Xu, K. Amine, *Nano Energy* **2023**, *115*, 108753.
[91] X. Du, Y. Gao, Z. Hou, X. Guo, Y. Zhu, B. Zhang, *ACS Appl. Energ. Mater.* **2022**, *5*, 2252–2259.
[92] M. D. L. Garayt, L. Zhang, Y. Zhang, M. C. Obialor, J. Deshmukh, Y. Xing, C. Yang, M. Metzger, J. R. Dahn, *J. Electrochem. Soc.* **2024**, *171*, 070523.
[93] C. Kim, H. Kim, M. K. Sadan, M. Jeon, G.-B. Cho, T.-H. Nam, K.-K. Cho, J.-H. Ahn, H.-J. Ahn, *J. Alloys Compd.* **2021**, *886*, 161240.
[94] a) H. Tan, D. Chen, X. Rui, Y. Yu, *Adv. Funct. Mater.* **2019**, *29*, 1808745; b) F. Legrain, O. I. Malyi, S. Manzhos, *Comput. Mater. Sci.* **2014**, *94*, 214–217.
[95] Y.-S. Choi, Y.-W. Byeon, J.-P. Ahn, J.-C. Lee, *Nano Lett.* **2017**, *17*, 679–686.
[96] S. Sarkar, A. Verma, P. P. Mukherjee, *J. Electrochem. Soc.* **2021**, *168*, 090550.
[97] C. Van der Marel, A. Van Oosten, W. Gertsma, W. Van der Lugt, *J. Phys. F* **1982**, *12*, 2349.
[98] S. Matsunaga, S. Tamaki, *J. Phys. Soc. Jpn.* **1983**, *52*, 1725–1729.
[99] W. Calaway, M.-L. Saboungi, *J. Phys. F* **1983**, *13*, 1213.
[100] J. Park, J. Han, J. Gim, J. Garcia, H. Iddir, S. Ahmed, G.-L. Xu, K. Amine, C. Johnson, Y. Jung, *Chem. Mater.* **2023**, *35*, 4171–4180.

Manuscript received: December 31, 2024
Revised manuscript received: March 4, 2025
Accepted manuscript online: March 13, 2025
Version of record online: March 25, 2025